J. Indian Inst. Sci., July–Aug. 1992, **72**, 315–367

IISc THESES ABSTRACTS

Thesis Abstract (Ph.D.)

Numerical analysis of dissociation nonequilibrium of gas phase in gas–particle nozzle flows by C. K. Baruah.
Research supervisor: N. M. Reddy.
Department: Aerospace Engineering.

1. Introduction

Many efforts have been made in the past to obtain solutions for the one-dimensional expansion of high-temperature gas–particle mixtures through convergent–divergent nozzle, which include both approximate analytical and exact numerical solutions. The techniques adopted in these studies are adequate to predict the temperature and velocity slips between the phases which exist due to the phase nonequilibrium prevailing in the gas–particle nozzle flows. However, in addition to the phase nonequilibrium, the gas–particle nozzle flow is often accompanied by relaxation phenomena, such as vibrational, dissociation, and ionization of gas molecules at high temperatures. The problem of such a complex flow has not been analysed.

This work deals with the analysis of one-dimensional gas–particle nozzle flow with dissociation nonequilibrium prevailing within the gas phase. The effect of the size of the particles and the loading ratio on the flow properties in the contour nozzle are discussed in detail.

2. Governing equations

The flow of dissociated oxygen gas seeded with dust particles expanding through a contour nozzle is considered. The dissociation and recombination processes in the oxygen gas are represented by,

$$O_2 + M_2 \underset{K_R^{(j)}}{\overset{K_F^{(j)}}{\rightleftharpoons}} 2O + M_j \tag{1}$$

where M_j is a collision partner ($M_1 = O$ and $M_2 = O_2$ in the present case), K_F and K_R are the forward and backward reaction rates.

The vibrational energy is assumed to be in equilibrium with the translational and rotational energies at the local gas temperature. The governing equations for one-dimensional unsteady gas flow through nozzles with dissociation nonequilibrium are given by Anderson[1]. The inclusion of solid particles in the flow will modify the set of governing equations with added interaction terms and additional conservation equations for the particle phase. The drag and heat-transfer coefficients and the gas–particle mixture viscosity are considered in the form given by Gottlieb and Ritzel[2] and Gottlieb and Coskunses[3]. The set of equations governing the flow are described in a recent paper by Reddy *et al*[4].

3. Results and discussion

The coupled nonlinear partial differential equations, governing the unsteady gas–particle nozzle flow with dissociation nonequilibrium of the gas phase are solved numerically using a time-marching technique which

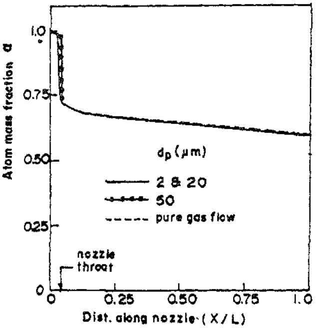

Fig. 1. The dependence of atom mass fraction on the particle dia. $\eta = 0{\cdot}5$, $P_0 = 81$ atm, and $T_0 = 5900$K.

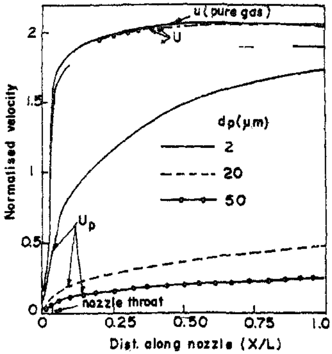

Fig. 2. The dependence of gas (u) and particle (u_p) velocities on the particle dia. $\eta = 0{\cdot}5$, $P_0 = 81$ atm, $T_0 = 5900$ K.

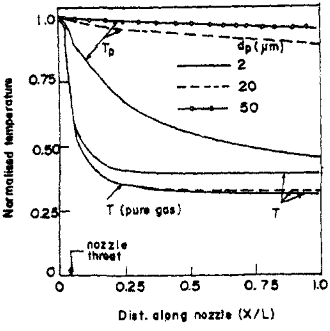

Fig. 3. The dependence of gas (T) and particle (T_p) temperatures on the particle dia $\eta = 0{\cdot}5$, $P_0 = 81$ atm, and $T_0 = 5900$ K

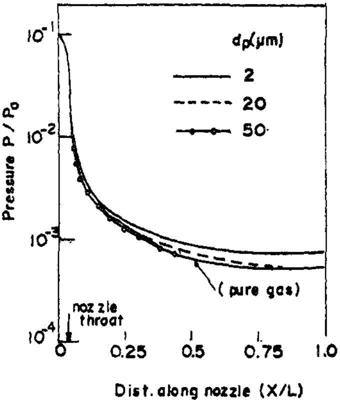

Fig. 4. The dependence of pressure on the particle dia. $\eta = 0{\cdot}5$, $P_0 = 81$ atm, and $T_0 = 5900$K.

entails the finite-difference solution of the unsteady equations in steps of time, starting from assumed initial distributions of the flow-field variables throughout the nozzle. The steady-state nonequilibrium nozzle flow solutions are approached at large times. The effects of particle diameter (d_p) and the loading ratio (η) on the flow parameters are studied in a contour nozzle.

Typical steady-state distribution of flow-field parameters obtained by solving unsteady governing equations numerically are presented in graphical form in Figs 1–4. The distributions of atom mass fraction, velocities, temperature and pressure of the gas–particle mixture along the length of the contour nozzle at loading ratio $\eta = 0{\cdot}5$ and different particle diameters are shown in Figs 1–4. It is observed, in Fig. 1, that the atom mass fraction decreases suddenly at the nozzle throat and remains frozen downstream. This is due to sudden expansion of the flow downstream of the nozzle throat resulting in fast cooling of the gas phase in the contour nozzle. This leads to freezing of molecular collisions which results in freezing of atom mass fraction.

The velocity distributions given in Fig. 2 show that a significant velocity slip between particle and gas phases develops even in the subsonic region of the nozzle and the slip in this region increases with the increase of particle size. The velocity slip reaches a maximum value immediately downstream of the throat and reduces towards the exit of the nozzle for 2-μm-size particles. However, for large-size particles the decrease of the slip towards the nozzle exit is negligible.

Steady-state distributions of temperature of the gas and particle phases along the axis of the nozzle for different particle diameters at loading ratio $\eta = 0{\cdot}5$ are shown in Fig. 3. The temperature (T) of the gas phase in gas–particle nozzle flow is higher than the corresponding temperature of the pure gas flow for smaller particle diameters. This is due to the fact that in the former case the expansion is slower than in the latter. It is also evident from this figure that a large temperature slip exists between the gas and particle phases. The large slip noticed near the throat is due to the sudden flow expansion with flow characteristic time smaller than the characteristic time of particle relaxation. The slip increases with the increase of particle diameter due to frozen flow conditions. This implies that the heat transfer from the particle phase to the gas phase is negligible at large particle diameters.

The steady-state pressure distributions of the gas–particle flow along the axis of contour nozzle are shown in Fig. 4 for different particle diameters at $\eta = 0{\cdot}5$. These results show that the pressure distribution tends towards that of pure gas nozzle flow for large particle diameters. The effect of loading ratio η at a fixed particle diameter on the atom mass fraction is also studied and detailed results are presented in the thesis. It is observed that as the loading ratio is increased the gas–particle mixture becomes heavy and less compressible as a result of which the flow moves towards that of isothermal and subsonic states.

4. Conclusions

The gas–particle nozzle flow with dissociational nonequilibrium of gas phase has been analysed. The steady-state distributions for the atom mass fraction, velocities, temperatures and pressure of the gas and particle phases along the axis of a conical nozzle are computed. The analysis shows that the atom mass fraction of the gas phase in gas–particle nozzle flows is unaffected by the presence of particles, irrespective of their size at low loading ratio ($\eta \leq 0{\cdot}5$). The atom mass fraction variation along the nozzle tends towards the frozen limit as the loading ratio increases.

References

1. Anderson, J. D. Jr	A time-dependent analysis for vibrational and chemical nonequilibrium nozzle flows, *AIAA J.*, 1970, **8**, 545–550.
2. Gottlieb, J. J. and Ritzel, D. V.	*A semi-empirical equation for the viscosity of air*, DRES Suffield Tech. Note No. 454.
3. Gottlieb, J. J. and Coskunses, C. E.	*Effects of particle volume on the structure of the partly dispersed normal shock wave in dusty gas*, UTIAS Rep. No. 295.
4. Reddy, N. M., Reddy, K. P. J. and Baruah, C. K.	Analysis of vibrational non-equilibrium of gas phase in gas–particle nozzle flows, *J. Aero. Soc. India*, 1990, **42**, 229–237.

Thesis Abstract (Ph.D.)

Fatigue crack closure under controlled stress intensity and temperature exposure by

K. K. Brahma.

Research supervisor: B. Dattaguru.

Department: Aerospace Engineering.

1. Introduction

With the increased emphasis on 'fail-safe' or 'damage tolerant' design of high-performance aerospace structures, the ability to accurately predict fatigue crack growth life in structural components has acquired importance. Attempts to predict variable amplitude crack growth from constant amplitude crack growth rate data wihout consideration of load interaction effects generally fail. A review of various methods available to model fatigue crack growth reveals that the method based on the well-known crack-closure phenomenon appears to be the best as it can lead to prediction of a large number of observed phenomena. This work provides a detailed study of crack-closure phenomenon and load interaction effects under various types of stress intensity-controlled fatigue testing with and without a single overload cycle.

2. Experimental programme

Automated fatigue testing facility was used for K-controlled—K-constant, K-increasing (constant stress amplitude) and K-decreasing — crack-growth tests. A crack mouth-opening displacement (CMOD) gauge was designed, fabricated and calibrated for crack length measurement. Crack length measurements were validated by using specially designed marker loading which leaves markings on the fracture surface. The marker spacings were measured using an optical microscope.

An improved technique for processing of load *vs* CMOD measurement data was developed for estimation of crack-closure/opening stress level. Crack-closure stress values thus obtained were validated by using an accurate fractographic technique[1].

3. Results and discussion

Typical variation of crack growth rate and S_{op}/S_{max} with respect to crack length for the case of constant K test with a single 100 per cent overload cycle is shown in Fig. 1. The crack-opening stress level has not come back to normal (expected value without overload) at 17 mm whereas the experimental growth rate shows that it has returned to normal. It means that at 17 mm the crack tip must have been fully open at 37 per cent of maximum load even though CMOD gauge estimates crack opening value of 64 per cent of maximum load. This apparent inconsistency can be resolved if it can be imagined that crack tip opens at 37 per cent of maximum load, but some other location in the wake still remains closed even up to 64 per cent of maximum load. One can expect that if the wedge action by the overload plastic zone in the wake is removed then the CMOD gauge will pick up the crack-tip-opening stress level. This fact was verified by drilling out the overload plastic zone in the wake when the growth rate came back to normal. Figure 1 also shows that the crack-opening stress level has dropped from 64 to 37 per cent of maximum load immediately after removal of the overload plastic zone. This confirmed that the CMOD gauge was indeed picking up the stress level at which the overload plastic zone in the wake was open rather than the crack-tip opening level. So it was successfully analysed that CMOD gauge measurements of crack closure could be erroneous after overload cycle, though the measurements were reliable for smoothly varying K tests. This observation explains the problems faced by some of the earlier workers[2] in interpreting fatigue crack growth and crack-opening stress level variations obtained with CMOD measurements.

Newman's crack closure model[3] was used with some modifications to study load-interaction effects. The rigid-perfectly plastic deformation along the crack line used by Newman was modified to elastic-perfectly plastic deformation. Using a similitude approach that the fatigue crack propagation would be similar for identical stress-intensity range, the fatigue crack growth in a single edge notched tension (SENT) specimen was simulated analytically in a center cracked tension (CCT) specimen. Predictions of crack opening stress levels and fatigue crack growth under K-controlled conditions made using the model were compared with test results obtained in the experimental programme.

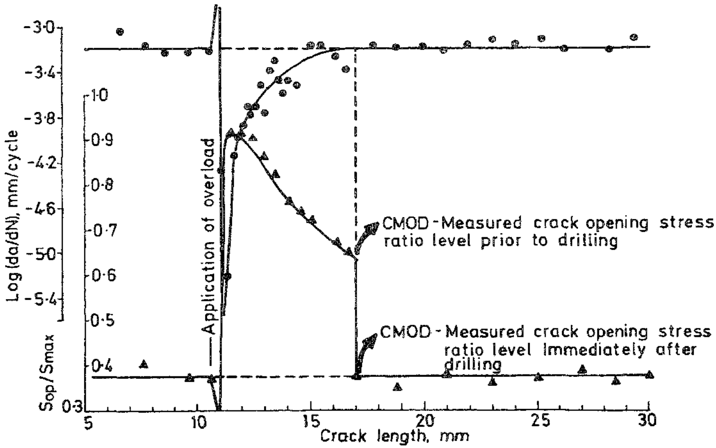

FIG. 1. Effect of drilling out the overload plastic zone on CMOD-measured crack-opening stress ratio: constant k test.

Effect of temperature exposure on fatigue crack growth retardation due to the application of an overload cycle was analysed. Temperature effects at zero applied stress were analytically modeled based on stress relaxation due to creep. During exposure to elevated temperature, the elastic strain due to residual stresses is converted to creep strains thereby decreasing the crack-opening stress levels. Acceleration of crack growth rate is explained by this model. Qualitative comparisons between experimental data and analytical model are found to be good.

4. Conclusions

The following conclusions have been drawn from this investigation:

a. A crack mouth-opening displacement (CMOD) gauge can be used to measure crack tip closure/opening stress level under smoothly varying load sequences, such as K-increasing, K-constant or K-decreasing tests. However, for a large (100 per cent in these experiments) overload cycle superimposed on smoothly varying K function, CMOD gauge-measurements do not necessarily provide the crack tip-opening stress level. In such cases, one should be careful in using CMOD gauge-measured crack closure in correlating fatigue crack growth.

b. The reduction in residual compressive stresses and hence crack closure due to temperature exposure could explain the effect of decrease in the retardation produced by overload cycle.

References

1. SUNDER, R. AND DASH, P. K.	Measurement of fatigue crack closure through electron microscopy, *Int. J. Fatigue*, 1982, **4**, 97–105.
2. VECCHIO, R. S., CROMPTON, J S. AND HERTZBERG, R. W.	Anomalous aspects of crack closure, *Int. J. Fracture*, 1986, **31**, R29–R33.
3. NEWMAN, J. C. Jr	*A crack closure model for predicting fatigue crack growth under aircraft spectrum loading*, ASTM STP 748, 1981, pp 53–84.

Thesis Abstract (Ph.D.)

A study on hygrothermal effects on advanced composites and adhesively bonded joints

by R. Gopalan.
Research supervisors: B. Dattaguru, T. S. Ramamurthy and Gangan Prathap (NAL).
Department: Aerospace Engineering.

1. Introduction

Composite materials are being increasingly used for structural applications in aerospace vehicles. These materials have numerous advantages such as high specific strength and stiffness, ability to tailor to desired strength and stiffness in different directions and improved fatigue resistance. In spite of these advantages, one could identify several gray areas before these materials could be used confidently in the primary structural components. One such area relates to the effect of exposure to hot, humid working environment, which could result in degradation of strength and stiffness of these materials. Therefore, the effect of moisture and temperature exposure on various advanced composites and their hybrids is studied. Extensive experimental programme was conducted to study the diffusion characteristics, degradation in mechanical properties of permeable and impermeable fibre composites and epoxy resin in thin film and bulk form and the failure processes with acoustic emission and scanning electron microscopic methods. Besides work on the basic materials, analytical and experimental studies on the effect of exposure to environmental conditions of composite–composite adhesively bonded joints is carried out. Significant aspect of this study is the development of methods to predict the strength of adhesively bonded joints using an average stress criterion on the stress distribution near the ends of the lap length.

2. Materials

The materials used in the present study are GFRP, CFRP, KFRP, C/GFRP and C/KFRP composites and epoxy resin (LY556 + HT972) as matrix material and adhesive in bonded joints. Out of these, the Kevlar fibre is a permeable fibre which absorbs moisture, whereas CFRP and GFRP are impermeable fibres. Based on the current-day acceptance standards, it was decided to study the maximum degradation of composites in fully saturated moisture conditions. The temperatures used for the study are fixed at room temperature and 70°C.

3. Experimental

The experimental work was initiated with studies on the diffusion characteristics of various composite materials to estimate the maximum moisture content and the time to reach moisture saturation (Fig. 1). Experiments were conducted on all the composites and their hybrids to check the adequacy of Fick's law of diffusion. Within the range of the temperature considered, Fick's law was found to be adequate for both permeable and impermeable fibre composites and the time taken for saturation could be estimated on the basis of this analytical model[1].

The next important aspect dealt with is the degradation of mechanical properties of the composite materials and the resin system due to environmental exposure. The same epoxy resin system is used as matrix in composites as well as adhesive in bonded joints in the present work. So, it has become important to study the properties of the resin and their degradation due to environmental effects in both thin film and bulk form. A special torsional test rig was developed and used to determine hygrothermal effects on the shear strength and shear modulus of neat resin in thin form ranging between 0·1 and 0·5 mm thickness. The neat resin along with its mould could be exposed to environmental conditions and tested for degradation of the properties[2]. For the composite plates and resin in bulk form standard tests such as tensile test, short beam shear test and plate twist test were conducted with and without exposure to hot humid conditions[3]. The degradation in mechanical properties is found to be larger for Kevlar fibre composites. A typical range of loss in stiffness in KFRP is about 30 per cent and the loss in tensile strength in all composites is about 10–15 per cent. Further, acoustic emission (AE) monitoring during the tensile test and scanning electron microscopic (SEM) studies on the fracture surfaces of various composites were conducted to understand the failure mechanisms before and after exposure to environmental conditions[4,5].

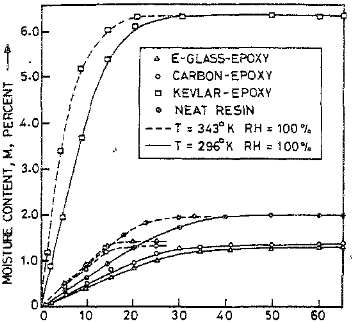

FIG. 1. Moisture absorption (%) *vs* time plot for permeable and impermeable fibre single composites.

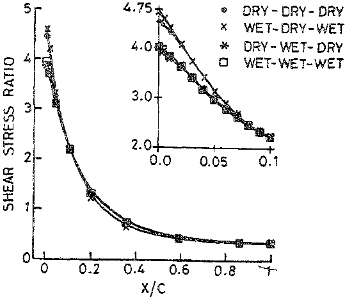

FIG. 2. Adhesive shear stress ratio distribution along lap length of CFRP–CFRP joint under different environmental exposures.

These studies have confirmed that exposure to environmental conditions results in change in the failure mechanisms from brittle to ductile. The studies also revealed excessive fibre pull out and fibre slipping in the exposed specimen showing considerable loss of the fibre matrix interfacial strength due to environmental exposure.

Adhesive bonding is preferred to mechanical fastening for joining composite structural components. Experiments were conducted to study the degradation of joint strength and change in the failure mechanisms in single lap-bonded joint with various composite adherends. Experimental studies were reported on dry–dry, wet–wet conditions of adherends and adhesive. The wet conditions correspond to full moisture saturation in both adhesive and adherends. The joints were tested to failure in tension and the failure mechanisms were studied by using AE and SEM techniques. Tensile tests have revealed degradation of about 13–20 per cent joint strength due to environmental exposure. The failure mechanisms in the joint showed predominant cohesive failure in the adhesive with certain regions near the ends of lap length showing interlaminar failure in the adherends in both exposed and unexposed joints. Acoustic emission results of cumulative counts *vs* load level was easily explained on the basis that failure mechanisms change from brittle to ductile due to environmental exposure.

4. FEM analysis

The final part of the work presented is on the finite-element analysis of adhesively bonded joints and method for prediction of joint strength. Single-lap adhesively bonded joints are known to undergo excessive rotation in the lap region due to eccentricity in the load-transfer path. A geometrical nonlinear analysis based on available software GAMNAS was used for this study. The shear stress and peel stress distribution along the lap length of the joint was determined for varied environmental conditioning of the adherends and adhesive[6]. Typical shear stress ratio *vs* lap lengths for CFRP–CFRP single-lap joint is shown in Fig. 2. The software was enhanced with pre– and post processors and modules for predicting the joint strength. The original and degraded properties of the composites and the neat resin in thin film form are used for the analysis. During the fabrication of joints a small spew was also noticed at the ends of the lap length, hence the spew was also modelled in the finite-element analysis. Since the dominant failure mode observed in the joints was cohesive adhesive failure, it was proposed to predict failure of the joints using the maximum shear stress criterion.

In two-dimensional plane-strain analysis of these joints, this criterion required a modification. The maximum shear stress value at the ends of the lap length obtained from the finite-element analyis was not reliable and in the absence of the spew, it could result in an unrealistic stress singularity. In order to overcome this, an average stress criterion was used. The stress distribution in the vicinity of the ends of the lap length was averaged over a characteristic length (a_o) and the average stress was compared with the shear strength to predict failure. The value of a was estimated such that the analytically predicted strength is equal to the experimental value. This characteristic length is nondimensionalised $(\bar{a}_o)$ with the lap length of the joint. The value of $\bar{a}_o$ estimated in all the joints had shown consistency. The value of $\bar{a}_o$ estimated is nearly equal to 3 per cent of the lap length and varies between 2·9 and 3·2 per cent for all the joints.

References

1. Gopalan, R. Murthy, M. V. V. and Dattaguru, B. — Diffusion studies on advanced fibre hybrid composites, *Reinforced Plast Composites*, 1986, **5**, 51–61 Also published in *Environmental effects on composite materials*, Vol. 3, edited by George Springer, Technomic Publishing Co., Lancaster, Pa, USA, 1988, pp 96–106.
2. Gopalan, R and Dattaguru, B — Hygrothermal effects on stress strain characteristics of thin adhesives, *Proc. Int. Conf. Structural Adhesives in Engineering*–II, University of Bristol, September 19–22, 1989, pp 107–111.
3. Gopalan, R Somashekar, B. R. and Dattaguru, B. — Environmental effects on fibre polymer composites, *J. Polymer Degradation Stability*, 1989, **24**, 361–371.
4. Gopalan, R. and Dattaguru, B. — Hygrothermal effects on the mechanical properties of advanced composites, *Proc. ICCM–7*, November 1–4, 1989, Beijing.
5. Gopalan, R Krishnan, R. V. and Venkataswamy, M. A. — Hygrothermal effects on failure process of advanced composites by SEM study, *Proc. ICSTAD*, IISc, Bangalore, July 29–Aug. 4, 1990, Vol. 2, pp 217–222.
6. Gopalan, R., Gangan Prathap and Dattaguru, B. — On the study of hygrothermal effects on composites and adhesively bonded joints, *Proc. Seminar on Science and Technology of Composites, Adhesives and Sealants*, Hindustan Aeronautics Limited, Bangalore, September 28–30, 1989, pp 327–335.

Thesis Abstract (Ph.D.)

Studies on reliability of reinforced concrete beams in cracking and ferrocement elements in tension and flexure by K. Balaji Rao.

Research supervisor: Prakash Desayi.
Department: Civil Engineering.

1. Introduction

Probabilistic analysis and development of reliability-based design formats is an active area of contemporary research. However, we have not come across in literature investigations dealing with probabilistic analysis of cracking in rc beams and strength and deformation of ferrocement elements. In the present study, Monte Carlo simulation technique is used to determine the statistical properties of variables considered. The cross-sectional dimensions, strengths of materials and prestressing force (in case of pretensioned ferrocement elements) are treated as random variables. The mean and nominal load and resistance factors are determined for a load and resistance factor design (LRFD) format using an advanced first-order second moment method. The form of the LRFD format chosen is,

$$\phi R > r_D D + r_L L \tag{1}$$

where R, D and L are resistance, dead load (effect) and live load (effect), respectively; ϕ, r_D and r_L are resistance, dead load and live load factors. The parameters considered in developing LRFD format are: (i) nature of live load distribution, (ii) coefficient of variation of live load, (iii) ratio of mean live load to mean dead load, and (iv) target reliability index.

2. Probabilistic analysis of cracking moment and reliability-based design of rc beams at limit state of cracking

2.1. From probabilistic analysis of cracking moment (M_{cr}) of 22 reinforced concrete beams, M_{cr} is found to follow normal distribution at 95 per cent confidence level. The degree of uncertainty associated with M_{cr} is noted to be significant compared to that of ultimate moment of rc flexural members. The proposed characteristic cracking moment (M^*_{cr}) equation is

$$M^*_{cr} = 0{\cdot}51\ \overline{M}_{cr} \tag{2}$$

where $\overline{M}_{cr}$ is the mean cracking moment.

2.2. From reliability-based design, it is concluded that both the nature and coefficient of variation of live load distribution do not have significant effect on resistance and load factors proposed.

3. Probabilistic analysis and stochastic modelling of cracking of rc beams

3.1. Three singly reinforced concrete beams of rectangular crosssection are tested under symmetrical third point loading. Strains, spacings and widths of cracks are measured at different stages of loading. From the probabilistic analysis of strains, crack spacings and crackwidths of three beams, it is found that: (a) the nature of probability distribution of strain at the level of steel depends on the magnitude of applied load, (b) nature of distribution of crack spacing and crackwidth depend not only on the magnitude of applied load but also on the way in which the steel is distributed in the tension zone.

3.2. Based on the results of probabilistic analysis of maximum crackwidths of 24 rc beams, a failure rate analysis method, which is consistent with the Monte Carlo and that takes into account the fact that cracking is a wear-out phenomenon, is proposed. Using this method, reliability of rc beams against limit state of crackwidth at various stages of loading is computed. The mean moment to failure determined using the proposed method are compared with the experimental values and satisfactory agreement obtained.

3.3. A nonhomogeneous Markov chain model is proposed to model the maximum crackwidth process in rc beams. The relevance of the model is justified and general equations for transition probabilities are derived. Assuming that maximum crackwidth at two successive stages of loading follows a joint Gaussian distribution, expressions for transition probabilities are derived. As an immediate application of the model, the maximum crackwidth states of three beams tested are predicted and satisfactory agreement is obtained with the test data. The model facilitates in the prediction of future state of cracking of the beam given its present state.

4. Probabilistic analysis of strength of ferrocement in tension

4.1. A total of 435 mesh wires have been tested in tension and from the statistical analysis of the test data it is noted that ultimate strength of mesh wires follows a two-parameter Weibull distribution.

4.2. The results of probabilistic analysis of cracking stress and ultimate load of 36 ordinary and 180 lightweight ferrocement specimens tested in tension[1] are compared with experimental values to propose equations for characteristic cracking stress and characteristic ultimate moment. The characteristic cracking stress equations for ordinary and lightweight ferrocement elements are obtained separately. The characteristic ultimate load (P^*_u) of ferrocement is given by,

$$P^*_u = 0{\cdot}764\ A_s\ \sigma_{su} \tag{3}$$

where A_s is the area of mesh wires running in the direction of applied load, and σ_{su} the ultimate strength of mesh wire.

4.3. Theoretical model to determine the upper and lower bounds for ultimate load are developed using classical chain-of-bundles concept. To determine the reliability of ferrocement, near ultimate expressions that take into account the number of bundles and the number of mesh wires in a bundle are derived.

5. Probabilistic analysis of ferrocement flexural elements

5.1. Deterministic methods are proposed to determine cracking moment (M_{cr}), ultimate moment (M_u), and load-deflection (P-δ) behaviour of ferrocement flexural elements using the test data of 37 specimens of shape and size normally encountered in practice. Out of 37 specimens, six are trapezoidal crosssection roofing elements[2], nine are channel crosssection floor elements[3], 16 are built-up I-joists[4], and six are monolithic I-joists (tested in the present investigation). Two methods are proposed to predict each of M_{cr} and M_u. A bilinear equation is proposed to compute short-term deflection. The computed M_{cr}, M_u and deflections under working loads are compared with their respective experimental values and satisfactory agreement is obtained.

5.2. Based on the observed strains and maximum crackwidth data of six monolithic I-joists tested in the present investigation, equations are proposed to determine strains, crack spacings and crackwidths in such sections.

5.3. From probabilistic analysis of M_{cr} and M_u (using both the methods) it is found that they follow normal distributions at 95 per cent confidence level. Equations for characteristic cracking moment (M^*_{cr}) and characteristic ultimate moment (M^*_u) are proposed. They are,

cracking moment:

$$\begin{aligned} M^*_{cr} &= 0{\cdot}74\,\overline{M}_{cr} \quad \text{(Method I)} \\ M^*_{cr} &= 0{\cdot}75\,\overline{M}_u \quad \text{(Method II)} \end{aligned} \tag{3}$$

ultimate moment:

$$\begin{aligned} M^*_u &= 0{\cdot}82\,\overline{M}_u \quad \text{(Method I)} \\ M^*_u &= 0{\cdot}83\,\overline{M}_u \quad \text{(Method II)} \end{aligned} \tag{4}$$

where $\overline{M}_{cr}$ and $\overline{M}_u$ are mean cracking and ultimate moments, respectively.

5.4. From probabilistic analysis of short-term deflection (δ), it is observed that δ at working loads follows log normal distribution at 95 per cent confidence level. The proposed characteristic short-term deflection (δ^*) equation is

$$\delta^* = 1{\cdot}349\,\bar{\delta} \tag{5}$$

where $\bar{\delta}$ is mean deflection.

5.5. Probabilistic analysis of crack spacings and crackwidths of ferrocement elements of different shapes considered is carried out. It is found that the nature of probability distribution of crackwidth is influenced by the presence of tension flange.

5.6. The resistance and load factors derived for LRFD format are presented in the form of tables and graphs. These can be used in the design of ferrocement flexural elements against limit state of collapse in flexure. It is noted that the values of resistance and load factors depend on nature and coefficient of variation of live load distribution.

6. Probabilistic analysis of pretensioned ferrocement elements

6.1. Probabilistic analysis of M_{cr} and M_u of six pretensioned and two non-prestressed trapezoidal roofing elements[5]; six pretensioned and two non-prestressed channel-type floor elements[6] is carried out. The effects of coefficient of variation of compressive strength of mortar (Ω_c) and coefficient of variation of prestressing force (Ω_l) on statistical properties of M_{cr} and M_u are studied. From this, it is found that: (i) the variations in Ω_c and Ω_l affect the nature of distribution of M_{cr} and M_u, (ii) M_{cr} of roofing and floor elements follows normal distribution at 95 per cent confidence level for various combinations of Ω_c and Ω_l, and (iii) for $\Omega_c = 0{\cdot}20$, and $\Omega_l = 0{\cdot}15$, M_u of roofing elements follows normal distribution at 99·9 per cent confidence level, while M_u of floor elements follows log normal distribution at 95 per cent confidence level.

6·2. The proposed equation for characteristic cracking moment (M_{cr}) of roofing and floor elements is

$$M^*_{cr} = 0{\cdot}69\ \overline{M}_{cr} \tag{5}$$

where $\overline{M}_{cr}$ is mean cracking moment. The characteristic ultimate moments (M^*_u) of roofing and floor elements are given respectively by

$$M^*_u = 0{\cdot}86\ \overline{M}_u \text{ (roofing elements)} \tag{6}$$

$$M^*_u = 0{\cdot}90\ \overline{M}_u \text{ (floor elements)} \tag{7}$$

where $\overline{M}_u$ is the ultimate moment.

6.3. Mean and nominal resistance and load factors are derived for LRFD format, for roofing and floor elements separately. The results are presented in the form of tables and figures. One of the conclusions drawn from this study is that the nature and coefficient of variation of live load distribution have significant effect on partial safety factors.

6.4. From the results of probabilistic analysis of short-term deflection (δ) of pretensioned roofing and floor elements, it is found that δ follows log normal distribution at 95 per cent confidence level. The characteristic deflection (d^*) is obtained as,

$$\delta^* = 1{\cdot}428\ \overline{\delta} \tag{8}$$

where $\overline{\delta}$ is mean deflection.

7. Conclusions

7.1. The above studies are expected to be useful in a better understanding of: (a) first crack strength and cracking of rc beams, (b) first crack and ultimate strengths of ordinary and lightweight ferrocement in tension, and (c) strength and behaviour of non-prestressed ferrocement elements.

7.2. The characteristic strength equations proposed will be useful in the analysis and design of members on a probabilistic basis.

7.3. The resistance and load factors obtained for LRFD format can be used in the design of elements, and can provide the information required in the formulation of Codes of Practice.

References

1. Desayi, P. and Reddy, V.	Strength and behaviour of lightweight ferrocement in tension, *Proc. Second Int. Symp. on Ferrocement*, Bangkok, Thailand, 1985, pp 61–73.
2. Desayi, P., Viswanatha, C. S. and Kanappan, S.	Some studies on ferrocement roofing elements, *J. Ferrocement*, 1982, 12, 273–288.
3. Desayi, P. and Ramesh, N. L.	Tests on ferrocement channel units, *Nervi Int. Symp. on Ferrocement*, RILEM, Bergamo, Italy, 1981, pp 2169–2177.

4. Desayi, P., Senthilnathan and Maheedhar Reddy, Y. — Application of ferrocement to roofing joists, *J. Instn Engr (India)*, 1985, **65** (C15), 215–221.

5. Desayi, P. and Reddy, V — Pretensioned ferrocement undulated roofing elements to cover long spans, *Proc. Int. Symp. on Innovative Applications of Shells and Spatial forms*, Bangalore, India, 1988, pp 809–819.

6. Desayi, P. and Reddy, V. — Pretensioned ferrocement floor elements of channel cross-section, *Proc. Third Int. Symp. on Ferrocement*, New Delhi, India, 1988, pp 314–323.

Thesis Abstract (Ph.D.)

Behaviour of electrically stressed thin silicon dioxide (SiO_2) films by K. S. Gurumurthy.
Research supervisor: M. Satyam.
Department: Electrical Communication Engineering.

1. Introduction

The importance of thin SiO_2 films is felt in many fields of semiconductor industry. The three major fields are: i) Short channel and sub-micron devices, ii) Large scale dynamic random access memories (DRAMs), and iii) Non-volatile electrically erasable programmable read only memories (EEPROMs). In all the above applications, reduction of gate oxide thickness is a must to improve the performance in metal oxide semiconductor (MOS) integrated circuits (ICs). Electrical breakdown of thin SiO_2 films is a major cause of circuit failure in large-scale DRAMs. In EEPROMs the rupture of the very thin tunnel oxides is the principle cause of write/erase (endurance) cycling failures. So a good understanding of the physical effects, resulting from the application of large electric fields applied to thin oxides is needed. Keeping this object in mind, three important investigations have been carried out in this work: i) Effect of electrical stress on the I–V characteristics of MOS diode, ii) Time-dependent oxide breakdown (TDOB), and iii) Post-breakdown characteristics of the MOS diode.

2. Reivew and experimental work

A good survey of research efforts in the thin SiO_2 films could be found in Beadle *et al*[1]. There are three well-known models explaining the breakdown mechanism in thin SiO_2 films[2–5]. Crystallographic distortion of the broken down oxide was studied through crosssection transmission electron microscope (XTEM) by Chou *et al*[6]. In this work, an effort is made to explain the TDOB characteristics and the post-breakdown characteristics by suitable theoretical and qualitative models, respectively.

The samples used were MOS diodes. They were fabricated by Semiconductor Complex Ltd (SCL), Chandigarh, India, using state of art of 3μm technology. The thermally grown oxide was 300Å in thick. HCl gas was used during the growth of oxide to reduce the mobile sodium ion concentration in the oxide. Aluminum was sputtered on both sides (after etching the oxide from the bottom side of the wafer) of the 10-cm dia wafer to take contacts. In the case of n-type wafer the bottom side of the wafer was implanted to get n^+ layer which facilitated to provide ohmic contacts with aluminum. Square gate electrodes were delineated using standard photolithography. The different square dots were i) $100 \times 100 \mu m^2$, ii) $200 \times 200 \mu m^2$, iii) $500 \times 500 \mu m^2$, iv) $1000 \times 1000 \mu m^2$, v) $2000 \times 2000 \mu m^2$.

3. Discussion and conclusion

V–I characteristics and TDOB characteristics of the sample were obtained using HP4145A (semiconductor parameter analyzer), high-frequency C–V characteristics were measured using HP 4061A (semiconductor/component test system).

V–I characteristics of the stressed samples were shifted to right. These are explained by the help of electrons and holes which were trapped in the oxide during electrical stressing. TDOB characteristics have been quantitatively explained. Change in potential profile of the oxide due to electron and hole trapping explains the decrease in current with time. Multiplication of carriers and subsequent charging of these carriers would enhance the internal fields. This charges the value of α (multiplication coefficient) which in turn increases the number of generated carriers. This is a cyclic process and when the internal fields reach a critical value, an avalanche of carriers is produced resulting in oxide breakdown. Thus, our model shows that both electrons and holes are responsible for the oxide breakdown. Mathematically computed characteristics match the experimental curves closely.

The post-breakdown characteristics obtained (*i.e.*, the V–I characteristics of the MOS sample after the oxide breakdown) were similar to a semiconductor rectifier in nature. The oxide undergoes a crystallographic distortion due to nucleation[6] during breakdown. The grown crystalline silicon due to nucleation was either single crystal or polycrystalline. This will lead to the formation of a junction at the interface of the grown crystal and the substrate. Since the grown crystal was like polycrystalline in nature, $\bar{p}$–n (or $\bar{p}$–p) junction was formed due to trapping of carriers in the polysilicon.

In summary, MOS samples with thermally grown 300Å-thick SiO_2 were subjected to electrical stressing and their V–I characteristics were studied. Experiments and the models revealed that the oxide contains both electron and hole traps. These traps are responsible for the breakdown of the oxide films. The post-breakdown characteristics show a p–n junction formation after the oxide breakdown which has been precisely attributed to nucleation and growth of silicon layers in SiO_2 layers.

References

1. Beadle; W. E., Tsai, J. C. C. and Plummer, R. D. — *Quick reference manual for silicon integrated circuit technology*, 1985, Wiley
2. O'Dwyer, J. J. — Theory of high-field conduction in a dielectric, *J. Appl. Phys.*, 1969, **40**, 3887–3890.
3. DiStefano, T. H. — Dielectric breakdown induced by sodium in MOS structures, *J Appl. Phys.*, 1973, **44**, 527–528.
4. Harari, E. — Dielectric breakdown in electrically stressed thin films of thermal SiO_2, *J. Appl. Phys.*, 1978, **49**, 2478–2489.
5. Chen, I. C., Holland, S. and Hu, C. — Hole trapping and breakdown in thin SiO_2, *IEEE Electron Device Lett.*, 1986, **EDL-7**, 164–167
6. Chou, T. C. and Tu, K. N. — Interaction of a polycrystalline silicon SiO_2/silicon substrates under thermal/electrical fields, *Appl. Phys. Lett.*, 1988, **52**, 1317–1319

Thesis Abstract (Ph.D.)

Hybrid technique for adaptive delta modulators by V. D. Mytri.

Research supervisor: A. P. Shivaprasad.
Department: Electrical Communication Engineering.

1. Introduction

To exploit the simplicity and excellent noise immunity characteristics of delta modulation (DM), several adaptive schemes have been proposed and applied to the basic invention[1,2]. While these coders (adaptive delta modulators) maintain simplicity, provide the best performance in the presence of random and independent channel errors and are less prone to quantizing noise, they have limited dynamic range due to slow attack/decay times.

2. HCFIDM and MCVSDM

The investigations carried out to develop new adaptation algorithms which enhance the dynamic range of these coders without affecting the other performance factors, have resulted in some versatile ADM systems, *viz.*, hybrid constant factor incremental delta modulators (HCFIDM) and modified continuously variable slope delta modulators (MCVSDM). The HCFIDM system combines the incremental type of instantaneous adaptation and the envelope type of syllabic adaptation. In the MCVSDM system, the syllabic filter exciting signal is made to vary as a function of the input signal level to provide slow changes in step size for small input levels and fast changes for large input levels.

The HCFIDM and MCVSDM systems have been studied on a digital computer with Gaussian signal, sine wave and digitized speech as the coder inputs, and also their performances compared to similar systems. The figure of merit used is the signal-to-noise ratio (SNR). With realistic values of the upper and lower limits of step sizes, a 55 dB dynamic range has been obtained as against 45 and 40 dB in the case of SVADM and CVSD coders, respectively. Effects of channel errors and tendem encoding are also studied. The performance in each case has been found to be equal to that of the CVSD system.

3. Results

Simulation results have been verified by building necessary laboratory models. Both objective and subjective testings have been carried out. Subjectively it has been observed that the HCFIDM and MCVSDM systems yield about 50 dB dynamic range at 32 kb/s as against 40 dB in the case of SVADM and the CVDM systems. At the same bit rate, the mean opinion score of HCFIDM and MCVSDM systems is approximately four on a five-point rating scale.

References

1. Jayant, N. S. and Noll, P.	*Digital coding of speech waveforms,* 1984, Prentice-Hall.
2. Un, C. K., Lee, H. S. and Song, J. S.	Hybrid companded delta modulation, *IEEE Trans.*, 1981, **COM-29**, 1337–1343.

Thesis Abstract (Ph.D.)

Studies on dc reactive magnetron sputtering—Preparation and characterization of Cu–Cu_2O cermet films by G. Mohan Rao.
Research supervisor: S. Mohan.
Department: Instrumentation and Services Unit.

1. Introduction

Cermets are metal–insulator composites[1] whose properties can be tailored by controlling the metal–insulator ratio. They are prepared in thin film form either by co-deposition of metal and insulator or by physical deposition of the metal in the presence of a reactive gas. Glow discharge sputtering is one such physical deposition technique. Problems of low deposition rate, rise in substrate temperature that are associated with normal dc sputtering can be solved by adopting magnetron sputtering technique[2], apart from target poisoning which is common during dc-reactive sputtering.

The present investigation is broadly divided into three distinct studies. Firstly, a magnetron cathode with high target utilization, high deposition rates, lower operating pressure and low substrate heating has been designed and its performance evaluated. The process of reactive sputtering of copper in oxygen and argon atmosphere has been studied at different oxygen partial pressures. This study gave an insight into the interdependence of the process parameters. Secondly, using the reactive sputtering process, cermet films of Cu–Cu_2O have been prepared and characterized for electrical and optical characteristics. Thirdly, cermet films have been studied for spectral-selective behaviour by measuring their solar absorptance and thermal emittance as a function of the composition. To measure thermal emittance accurately, a vacuum emissivity meter based on steady-state calorimetric technique has been designed and developed.

2. Experimental techniques

Magnetron sputtering has been carried out in a home-made vacuum system capable of reaching an ultimate

FIG. 1. Erosion zone of the magnetron target

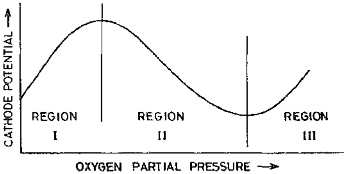

FIG 2 Variation of cathode potential as a function of oxygen partial pressure during dc-reactive magnetron sputtering

vacuum of 10^{-6} torr, and sputtering in the downward sputtering mode. High-purity argon (5N) and oxygen (4N) have been used as sputtering and reactive gas, respectively. Pressure monitoring has been done using a Pirani–Penning gauge combination calibrated using McLeod gauge against argon gas. Sheet resistance of the films has been measured using an inline four-probe technique. Optical characteristics of the deposited films have been measured using a double-beam spectrophotometer (Hitachi 330).

Structure and composition of the cermet films have been studied by x-ray diffraction and electron microscopy. The volume fraction of copper in the films has been determined by studying the electron micrographs in an image analyser system. This study can be erroneous, if the films are homogeneous. To study the homogeneity of the film composition, Auger electron spectroscopy has been carried out for some typical samples Depth analysis across the film thickness showed them to be homogeneous

3. Results

To study the effect of the magnetic field geometry on the performance of the magnetron, four different magnet geometries have been studied. Based on this study, it was found that a ring magnet with an extended pole piece geometry is more effective in achieving reasonably good characteristics. It also showed that the magnetic field strength decides the lowest operating pressure and the uniformity of field decides the uniformity of erosion. With the magnetron developed during this study[3], a deposition rate of 2000Å/min with a current density of 5 mA/cm^2 has been obtained at a pressure of 8×10^{-3} torr. The substrate temperature rise under this condition is only 40°C as compared to 450°C at a lower current density and higher operating pressure in normal dc sputtering. Maximum uniformity in deposited films has been achieved at an interelectrode distance of 60 mm and above. The erosion zone constituted more than 75 per cent of the target area (Fig. 1). Reactive sputtering in argon and oxygen mixtures resulted in interesting changes in the glow-discharge characteristics. As the oxygen partial pressure is increased, the cathode potential required to achieve a particular current density increased, up to a critical oxygen partial pressure, beyond which it decreased. This is contrary to the results generally reported. It is normally observed that addition of even a small quantity of oxygen in the system resulted in reduction of cathode potentials at any current[4]. The anomalous behaviour of cathode potentials has been explained on the basis of negative ion formation and cathode poisoning effects. Due to negative ion formation depletion of electrons takes place and this causes an increase in cathode potentials initially. After a critical oxygen pressure is reached, target poisoning starts and since the oxide has higher electron emission, the cathode potentials reduce; once the target poisoning is complete, the cathode potentials again increase. This is explicable because higher voltages are required to break the insulating layer and sustain the discharge (Fig. 2).

Homogeneous cermet films of Cu–Cu_2O have been prepared[5] with good control over composition. At an oxygen partial pressure of 10^{-4} torr and a total sputtering pressure of 10^{-2} torr, the volume fraction of copper reduced from 88 to 27 per cent, when the deposition was varied from 1200 Å/min to 525 Å/min. This resulted in good control on the electrical and optical characteristics of the deposited films. The sheet resistance varied from 10 ohms/sq to a few kilo ohms/sq, optical transmittance varied from 1 to 70 per cent. Cermets exhibited spectral selectivity and have good absorption in the solar spectral region. Selectivity was found to be dependent on the volume fraction of the metal present in the film. Good absorbing films are found to have a metal volume fraction of about 20 per cent and are stable up to 150°C in air.

Modifications made on steady-state calorimetric technique[6] resulted in measurement of emittance to an accuracy of ± 0·02 and the experimental time is about one hour, as compared to several hours reported earlier.

4. Conclusions

This investigation resulted in an understanding of the requirements for the designing of planar magnetrons. The importance of magnetic field strength and uniformity in reducing substrate heating and achieving high deposition rates has been established. Homogeneous cermets have been prepared with good control over the composition. It has been shown that magnetron sputtering minimises the target poisoning effect. The glow-discharge characteristics in reactive sputtering resulted in a new explanation for the process. By considering simple experimental facts, the measurement of emittance using a vacuum emissivity meter has been made rapid and accurate.

Reference

1. MEIKSIN, Z H	In *Physics of thin films*, Vol. 8, (ed , G. Hass, M H. Francombe and R. W. Hoffman), 1975, Academic Press
2. WAITS, R K.	*J. Vacuum Sci. Technol*, 1978, **15**, 179–187.
3. MOHAN RAO, G. AND MOHAN. S.	*Vacuum*, 1990, **40**, 313–314.
4. MAISSEL, L.	In *Handbook of thin film technology* (eds, L., Maissel and R. Glang), 1970, pp 4–28, McGraw-Hill.
5. MOHAN RAO, G., PANCHAPAGESAN, T. S. AND MOHAN, S.	*Appl. Phys. A*, 1990, **51**, 423–426.
6. MOHAN RAO, G. AND MOHAN, S	*Rev. Sci. Instrum* , 1988, **59**, 817–818

Thesis Abstract (Ph.D.)

Interorganisational technology transfer from research to manufacture: A field study of adoption in India by G. Balaji.

Research supervisor: K. N. Krishnaswamy.

Department: Management Studies.

1. Introduction

It is generally accepted that the application of scientific knowledge is the most effective path for the chronically underdeveloped countries to achieve socio-economic development. This is the basic premise for technology development programmes the world over. However, over the last few decades, these programmes in most countries have hardly been successful. Both the production of scientific knowledge and its diffusion into the economy have not reached levels wherefrom material progress of the people of the country could be accomplished. Despite huge investments in national R&D in India, its effect on Indian industry has not been very significant[1]. This state of affairs has led to a decadence of the institution of indigenous research and to consequent questions about its very necessity. Investigation into the reasons for the ineffectiveness of indigenous research and halting this erosion of credibility in it, thus, assumes paramount importance.

While problems of technological choice, project selection and R&D management are encountered in the production of scientific knowledge, socio-economic, technical and behavioural barriers have to be contended with in its application to all forms of human activity. The latter have been referred to as the problems of technology transfer (TT). This work undertakes to investigate some of these problems.

2. Perspectives of the study

The study envisages three basic entities of the process of TT—the donor system, the receiver system and a mode of interaction between them. These entities have been used to develop an exhaustive taxonomy of TTs. Based on a few case histories of TT in India, interorganisational TT is postulated as a subprocess in the process of technological innovation. Further, the TT process is considered as the process of effecting a shift in the managerial control over the innovation process during some point in the time period spanned by the innovation process. As a consequence of this, it is useful to consider the process of TT, not in isolation, but as a part of an overall non-integrated innovation process.

Therefore, in order to understand the process of TT from government-aided laboratories to industry in India, considering it as a part of the non-integrated innovation process, it is necessary (a) to identify those variables and factors that significantly differentiate between successful and failed TTs; (b) to test various hypotheses available in the literature on innovation and TT in the Indian environment; and (c) to suggest procedural and policy changes based on the results. These are the objectives of this work.

An adopter-oriented model of the process of TT is proposed. Three groups of variables, totaling 40, are identified as potentially important ones affecting this process; of these, 16 are firm-related variables, one is a technology-related variable and 23 are contextual variables.

3. Research design

A field of 100 cases of TT in India was conducted and information on these variables was obtained through a questionnaire. Method of data collection was both through mailed questionnaires and personal interviews. In order to meet the objectives of the study the data were subjected to three independent analysis; a pair-wise comparison analysis[2], a factor analysis and discriminant analysis of 86 cases of TT[3] and a correlational analysis of 86 cases of TT[4]. For the pair-wise comparison 30 success-failure pairs of instances of technology transfer (for the same technology) were identified. Pairing of TT cases enabled the control of technology-related variables.

4. Results

The pair-wise comparison analysis identified 24 variables that significantly differentiated successful and failure cases. Differences in the set of significant variables for product and process innovations were also observed. These differences arising out of the size of the recipient firms, the market structure under which they operate and the extent of technology and market determinateness of product and process technologies, imply the need for a differential treatment of product and process TTs by managers. This result was reiterated by the correlational analysis working under a different set of statistical assumptions.

The success of the delicate operation of transferring a partially developed technology from one organisation to another is based on a good 'fit' between the donor and the recipient organisation in terms of project objectives, personnel, and technical skills. These contextual variables are major factors that affect the process of technology transfer. The results of the analyses clearly bring out the predominance of contextual variables. The perceived stage of development of the technology is an important variable in both product as well as process technologies. Firm-related variables like technical progressiveness, management strength, and innovative marketing, were found to be good predictors of success in technology transfer. The results of factor analysis resulted in the definition of nine 'real' factors that significantly affected the process of technology transfer. A multiple discriminant analysis using these factors correctly classified over 75 per cent of the cases. The implications of these results for the donor of the technology (like the funding procedure for R&D projects in laboratories) are discussed. For the recipient of the technology, the implications of these results are the need for efficient coordination between the different elements and organisations involved in each of the TT process.

References

1. Desai, A	The origin and direction of industrial research in India, *Res. Policy*, 1980, **9**, 74–96.
2. Sappho	*Success and failure in industrial innovation: Report on Project SAPPHO*, Centre for the Study of Industrial Innovation.
3. Bar-Zakay, S N.	Technology transfer from defence to civilian sector in Israel: Methodology and findings, in *Industrial technology transfer*, Cetron, M. J. and Davidson, H F. (eds),1977, pp 217–244, Noordhoff.
4. Chakrabarthi, A. K. and Rubenstein, A. H.	Interorganisational technology transfer: A study of adoption of NASA innovations, *IEEE Trans.*, 1976, **EM-23**, 20–34.

Thesis Abstract (Ph.D.)

Transonic flow in a rotating turbine cascade of large pitch to chord ratio by M. V. A. Murthy.
Research supervisors: S. Soundranayagam and Pramod A. Paranjpe (NAL).
Department: Mechanical Engineering.

1. Introduction

The simulation of high-stagger low-turning turbine cascades with supersonic exit Mach numbers in a stationary plane cascade tunnel poses problems like achieving periodicity of exit flow and measurement in a supersonic flow field. Such turbine cascades can be conveniently simulated in a rotating rig and the measurements made in the absolute frame of reference by stationary probes in the subsonic flow field. However, in rotating cascade tests, there are a large number of problems that have to be considered in the evaluation and analysis of the results.

Radial traverse measurements downstream of rotating turbine cascades at high Mach number[1] show a very narrow region of flow free from annulus boundary layer. Even in the flow region away from the annulus boundary layer, the axial velocity density ratio (AVDR) across the cascade could be different from 1·0 showing that the flow is not two dimensional. In the high Mach number range the variation of AVDR and its associated effects could be large. Such effects have been noticed during the past in stationary cascade tunnels[2,3], but no results are available on the magnitude of AVDR variation in rotating turbine cascades to assess its effects with reference to 2D flows. A high-speed rotating turbine cascade was built and detailed measurements made to investigate the effects of non-two dimensionality.

The measurement of internal flows in a rotating cascade will be affected by wall proximity effects on the probe readings. Such wall proximity effects have been noticed by some workers[4,5] in probe calibration rigs, but little if any information is available on their effect in an actual turbomachine. Special attention was paid in this study to evaluate the effects of wall proximity on the results.

2. Program of work

Experimental investigations were carried out in a high-speed rotating turbine cascade of high-stagger low-turning blades designed to simulate nearly two-dimensional flow, over a range of test conditions corresponding to blade incidence varying from 0 to 6 degrees and the relative outlet flow Mach number varying from 0·75 to 1·25. The setting of the incidence angle and the relative outlet flow Mach number during the tests was achieved by a proper combination of the flow rate through the cascade and the rotating speed.

The measuring probes were calibrated in a specially built calibration rig over a range of flow Mach numbers with the probe head at different distances from a wall. The results of these calibrations were incorporated in the data reduction program to take wall proximity effects into account in the cascade evaluation.

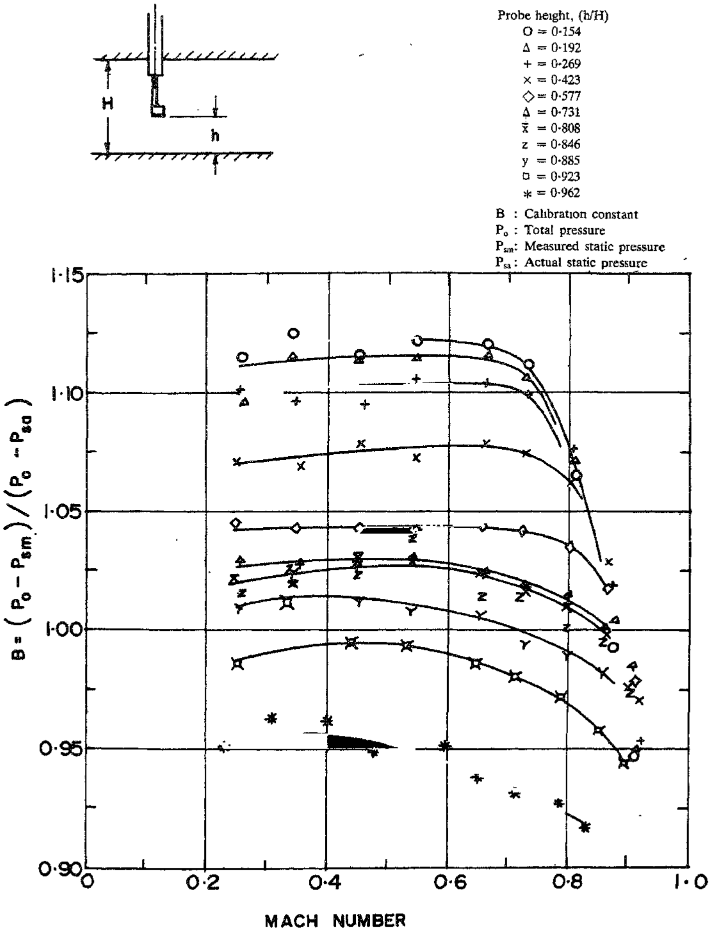

FIG. 1. Wedge probe constant variation as a function of Mach number and probe height (probe 1).

For all the tested conditions of the rotating cascade, the local flow parameters along the blade height were initially evaluated by the method of Lawaczeck[1] which neglects the non-two-dimensional flow effects by assuming AVDR = 1. The data evaluation method of Lawaczeck[1] was extended to include the effects of the measured AVDR across the cascade and these results were compared with detailed measurements of the variation of flow angle and Mach numbers, etc., along blade height.

The pressure field at the tip relative to the blade was evaluated from traverse measurements of unsteady wall static pressure by a rapid response transducer. These results were compared with theoretical predictions based on the solution of the stream function equation by a finite difference technique.

3. Results and discussion

The studies have shown that wall proximity has strong effects on the probe constants as seen in Fig. 1. The calibration data presented in Fig. 1 show that the presence of the probe stem also has a strong effect resulting in the variation of the probe constant along the height of the channel being unsymmetric with respect to the channel mid-height.

Analysis of the rotating cascade measurements shows that wall proximity corrections have little effect on parameters like flow Mach number which depend on the ratio of pressures, while the neglect of wall effects in the evaluation of parameters like loss coefficients which depend on the difference of pressures resulted in errors to the extent of 12 per cent near the wall.

One of the most important results expected in a cascade test is the value of the outlet flow angle. Figure 2 shows a typical variation of the measured exit-relative flow angle along the blade height. Under all the tested conditions, similar trends of variation were observed where the exit angle reduced considerably towards the tip. The exit-relative flow angles were also evaluated by the method of Lawaczeck[1] and by the expression $\cos^{-1} o/s$ for gauging angle. As seen in Fig. 2 these methods fail to describe the experimental variation particularly near the tip where the AVDR increased steeply. These methods were then extended to include the effects of the locally measured AVDR. The results of the modified method showed good agreement with the measured angle at all blade heights (Fig. 2) and at all test conditions. The inclusion of AVDR effects in the expression for gauging angle improved the prediction, but is still inadequate to reproduce the measured values.

The measurements showed that the exit-relative angle decreased quite rapidly with AVDR. At locations near blade mid-height where AVDR was 1·0, the variation of exit-relative flow angle with eixt-relative Mach number conformed to the known correlations of 2D stationary cascade results. This suggests that when comparison of the results in rotating cascades is made with those in stationary cascades and 2D computations, it should be with measurements around the blade mid-height region of the rotating cascade at the radius which gives the same AVDR.

Figure 3 shows a typical pressure field relative to the blade at the casing wall obtained from traverse measurements of unsteady wall static pressure using a rapid-response transducer. This pressure field corresponds to an incidence angle of 6 degrees. The isobar contours plotted in Fig. 3 indicate a local shock on the suction surface smeared due to tip clearance flows. At higher flow Mach numbers the local shocks were found to be further smeared and swept downstream. Reduced incidence angles resulted in weaker shocks. The isobar contour in Fig. 3 shows a sonic line which is highly curved and crosses the flow passage behind the trailing edge. Similar sonic lines have been observed in a 2D stationary cascade tunnel at small supercritical pressure ratios across a high-pitch-to-chord-ratio turbine cascade[6].

The pressure field at the tip relative to the blade was also computed theoretically by solving the stream function equation. The computation was carried out for a stream thickness variation corresponding to the measured AVDR at the tip. The computed isobar contours were nearly normal to the blade surface. In comparison to this, the isobar contours obtained through measurements were distorted due to tip clearance flows and the contours of equal strength on either side of the blade surface joined together in the clearance gap running parallel to the blade chord (Fig. 3). Computations were also carried out on other profile sections for which experimental data were already available. The computation of the flow field past a VKI profile (Fig. 4) predicted shock locations is in good agreement with experiment with reference to the

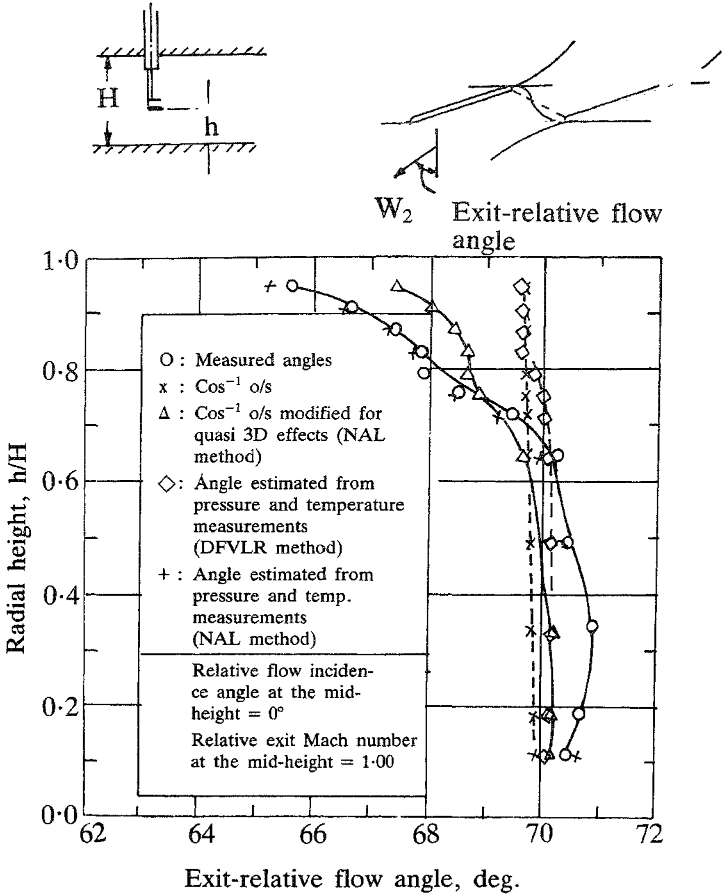

FIG. 2. Variation of exit-relative flow angle along the blade height.

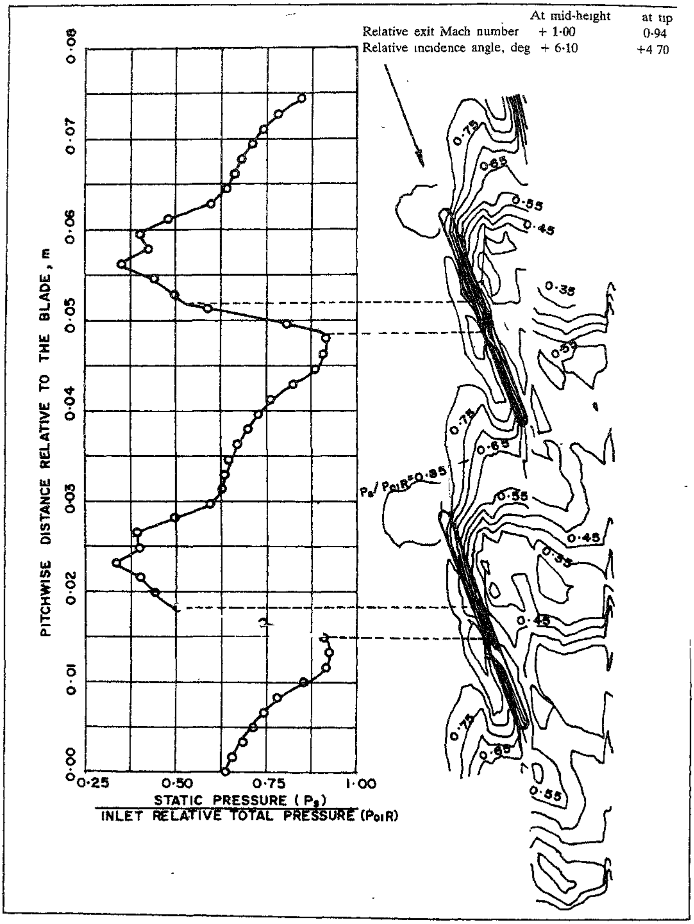

	At mid-height	at tip
Relative exit Mach number	+ 1·00	0·94
Relative incidence angle, deg	+ 6·10	+4 70

FIG. 3. Pitchwise static pressure variation at the blade mid chord location and ISO bar contours in the blade region at the tip (based on the measurements at the casing wall).

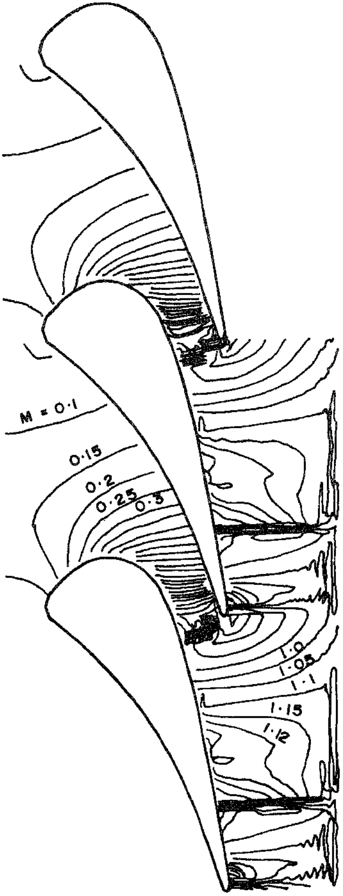

VKI nozzle profile
(ref. VKI LS 1982–05,
vol. 3)

FIG. 4. Calculated Mach number contours for exit Mach number of 1·05.

Schlieren photograph available in Sieverding *et al*[7]. The computed blade surface Mach number also was in agreement with experiments in the subsonic range of local Mach numbers, but showed over expansion in the transonic flow range. In the transonic flow range, since the flow is sensitive to the area changes, the inclusion of boundary-layer effects is expected to improve the predictions.

4. Conclusions

It has been clearly established in the present study that the effect of AVDR must be included in any data evaluation method that does not depend on a direct measurement of angle and static pressure and that measurement at the mid-span does not ensure that AVDR effects could be neglected. The inclusion of AVDR has given very good agreement with the measured angles at all points along the blade height and has also improved the evaluation of loss coefficient.

The study on the wall effects has shown that they have an important influence on the probe constant and that they should be taken into account in all internal flow measurements. The computational results point to the importance of including boundary-layer effects in the transonic Mach number range where the flow is very sensitive to area changes.

References

1. Heinemann, H.-J	Ein neues mess–und auswerteverfahren fuer untersuchungen an rotierenden ringgittern, *VDI–Forschungsheft*, 1979, **594**, 1–31.
2. Kiock, R., Lehthaus, F., Baines, N. C. and Sieverding, C. H.	The transonic flow through a plane turbine cascade as measured in four European wind tunnels, *J. Engng Gas Turbines Power, Trans ASME*, 1986, **108**, 277–284.
3. Starken, H. and Lichtfuss, H -J.	Some experimental results of two-dimensional compressor cascade at supersonic inlet velocities, *J Engng Power. Trans. ASME, A*, 1970, **92**, 267–274.
4. Beretta-Piccoli, F. and Fransson, T.	Probe investigations in the proximity of a wall in supersonic flow, *Proc. Symp. on Measuring Technique in Transonic and Supersonic Flows in Cascades and Turbines*, Lyon, 1982, pp 8–1 to 8–15.
5. Heneka, A. and Bubeck, H.	Measuring errors of pneumatic multihole-probes, *Proc. 7th Symp. on Measuring Technique for Transonic and Supersonic Flow in Cascades and Turbomachines*, Aachen, 1983, pp 14–1 to 14–14.
6. Sieverding, C. and Sampson, R.	The flow through low-cambered transonic turbine cascades, *VKI Short Course on Flow in Turbines*, April 1969, pp 1–23.
7. Sieverding, C. H., Van Hove, W., Boletis, E , Gotthardt, H. and Stark, V.	Description of test cases and presentation of experimental results, Vol. 3: *Workshop on 2D and 3D Flow Calculations in Turbine Blading, VKI Lecture Series* 1982–05, pp 1–61.

Thesis Abstract (Ph.D.)

Electrochemical aspects of interactions among ball materials and minerals with reference to grinding and flotation of complex copper–lead–zinc sulphides by M. K. Yelloji Rao.

Research supervisor: K. A. Natarajan.
Department: Metallurgy.

1. Introduction

Steel balls are being used for long as grinding media in mineral processing operations. During grinding, wear takes place due to abrasion, corrosion, impact and erosion. Several complex parameters involving composition, hardness and microstructure of the grinding media, hardness ratio of the ball to the mineral,

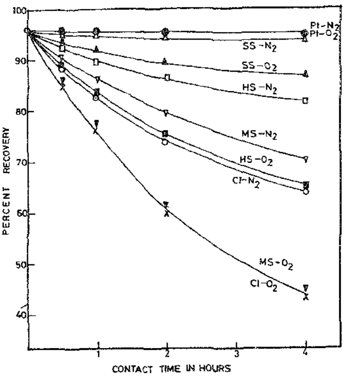

FIG. 1. Flotation recovery of chalcopyrite after contacting with different metallic materials under different aeration conditions (Pt: platinum, SS: stainless steel, HS: hyper steel grinding medium, MS: mild steel and CI: cast iron).

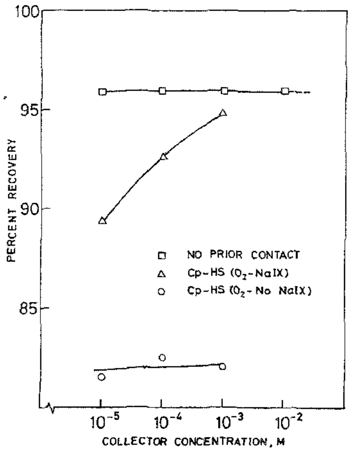

FIG. 2. Flotation recovery of chalcopyrite as a function of collector concentration added either during galvanic interaction with hyper steel or while conditioning after severing the contact (1h) in the presence and absence of galvanic interaction.

and mineral slurry pH, pulp density, conductivity and viscosity of the slurry are known to influence the media wear significantly[1-3]. Apart from the environment in a mill, electrochemical and magnetic interactions could also influence ball wear[4,5]. Besides contributing towards ball wear, possible interactions between balls and minerals on the one hand and between mineral and mineral on the other could also affect the electrochemical and surface chemical properties of individual sulphides, thus influencing their subsequent response to flotation[6,7]. The present study has therefore been addressed to electrochemical aspects of grinding and flotation of complex sulphides since a basic understanding of the electrochemical behaviour of sulphides such as chalcopyrite, sphalerite and galena when present either individually or in various possible combinations would have practical implications in the processing of complex copper–lead–zinc sulphides.

Major objectives of the present study therefore include:

1. Investigations on the effect of single mineral–grinding media galvanic interaction on the flotation of chalcopyrite, sphalerite and galena.
2. Studies on the role of mineral–mineral interaction as distinct from that of grinding media–mineral interaction on sulphide flotation with respect to chalcopyrite, sphalerite and galena in different possible combinations.
3. Examination of the influence of the presence of a grinding medium on different bi- and trimineral interactions, and
4. Assessment of the relative significance of grinding media wear during chalcopyrite ore grinding under different experimental conditions and its effect on flotation.

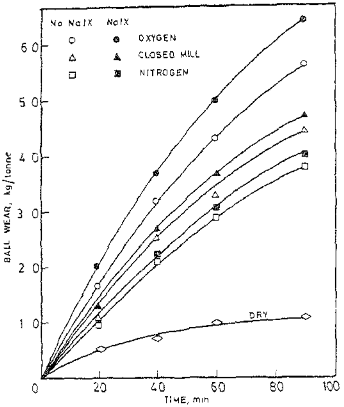

FIG. 3. Wear of hyper steel balls during chalcopyrite ore wet grinding as a function of time and different aeration conditions in the presence and absence of sodium isopropyl xanthate (NaIX) collector.

2. Experimental programme

Initial electrochemical studies were confined to the measurement of steady-state rest potentials for different sulphide minerals and ball materials both in the presence and absence of flotation reagents. Besides rest potentials, the combination potentials and galvanic currents under different mineral–mineral and mineral–grinding media couples were also measured. Marked ball grinding tests were carried out by using hyper steel balls and chalcopyrite ore.

Flotation tests after various types of galvanic interactions were carried out by using a Hallimond flotation cell. Bench-scale flotation tests were also carried out for chalcopyrite ore after grinding with hyper steel balls using a Denver flotation cell.

Surface analysis studies were carried out by using a) AES and ESCA, b) scanning electron microscopy, and c) cyclic voltammetry.

3. Main results and conclusions

The results indicate that prior galvanic interaction with the grinding media affects deleteriously the flotability of chalcopyrite mineral (Fig. 1). Similar observations were also made with other sulphide minerals such as sphalerite and galena. Surface analysis studies through ESCA and cyclic voltammetry indicated the presence of oxy-hydroxide species of iron on the interacted sulphides which alters the surface chemistry of the mineral. The decrease in floatability of the sulphide mineral after contacting with the ball material could therefore be explained on the basis of iron dissolution from the grinding media and its subsequent adsorption/deposition on the sulphide mineral. The influence of such galvanic effect on the floatability of a sulphide mineral is dependent on the duration of contact, as well as the presence or absence of oxygen and of flotation reagents. The adverse effect on sulphide mineral floatability also appears to be directly related to the extent of anodic iron dissolution from the grinding media. The presence of a collector at the time of galvanic contact helps in minimizing such a deleterious effect on chalcopyrite

Table I

Flotation recovery of chalcopyrite after wet grinding in the presence of added collector to the mill (hyper steel ball grinding)

Collector concentration added to the mill	*Per cent recovery*		
	N_2	*Closed mill*	O_2
–	34·1	18·8	13·1
10^{-5}M	38·0	22·9	18·3
10^{-4}M	53·4	45·1	35·6

(Fig. 2) and galena flotation, though not for sphalerite. In the case of sphalerite, the presence of a sufficient concentration of the activator alone during contact helps in minimizing such a deleterious effect.

Due to galvanic interactions among sulphide minerals, the floatability of a relatively active mineral in the combination was found to be only marginally affected, whereas that of the nobler mineral was found to be significantly lowered. The additional presence of a grinding medium during the above mineral–mineral contacts significantly lowered the flotation response of all the minerals. The formation of oxy-hydroxide species of iron on the sulphide minerals due to prior multimineral–grinding media electrochemical interaction was found to be dependent on the relative electrochemical activities of the minerals; more favoured on the noble minerals than on active minerals. However, accidental activation due to copper ions released from chalcopyrite and hence improved flotation recovery of sphalerite could be seen in bi- and trimineral combinations involving chalcopyrite, sphalerite, both in the presence and absence of grinding medium.

Grinding media–mineral interactions during chalcopyrite ore grinding contribute not only towards enhanced ball wear but also affect deleteriously the flotation response of the ground mineral. The simultaneous addition of collector during grinding, although increases the media wear (Fig. 3), was found to be beneficial from a flotation view point (Table I). Addition of chalcopyrite to quartzite in a wet-grinding mill leads to an increase in the corrosive wear of balls, especially in the presence of oxygen.

Electrochemical mechanisms and models are proposed to explain the effect of different types of binary and ternary mineral interactions on the bulk and differential flotation of multisulphides containing chalcopyrite, sphalerite and galena. The effect of the simultaneous presence of a steel ball material in the above mineral combinations is also examined from an electrochemical view point.

References

1. FUERSTENAU, D. W., VENKATARAMAN, K. S. AND VELAMAKANNI, B. V.	Effect of chemical additives on the dynamics of grinding media in wet ball mill grinding, *Int. J. Miner. Processing*, 1985, **15**, 251–267
2. MOYS, M. H. AND MONTINI, A.	The use of conductivity measurements in the control of grinding mills, *CIM Bull.*, 1987, **80**, 52–56.
3. MOORE, J. J., PEREZ, R. GANGOPADHYAY, K. AND EGGERT, J. F.	Factors affecting wear in tumbling mills: Influence of composition and microstructure, *Int. J. Miner. Processing*, 1988, **22**, 313–343.
4. NATARAJAN, K. A., RIEMER, S. C. AND IWASAKI, I.	Influence of pyrrhotite on the corrosive wear of grinding balls in magnetite ore grinding, *Int. J. Miner. Processing*, 1984, **13**, 73–81.
5. POZZO, R. L. AND IWASAKI, I.	An electrochemical study of pyrrhotite–grinding media interaction under abrasive conditions, *Corrosion*, 1987, **43**, 159–164.
6. ADAM, K., NATARAJAN, K. A. IWASAKI, I.	Grinding media wear and its effect on the flotation of sulphide minerals, *Int. J. Miner. Processing*, 1984, **12**, 39–54.
7. NAKAZAWA, H. AND IWASAKI, I.	Galvanic contact between nickel arsenide and pyrrhotite and its effect on flotation, *Int. J. Miner. Processing*, 1986, **18**, 203–215.

Thesis Abstract (Ph.D.)

Studies on 3-hydroxybenzoate-6-hydroxylase in *Micrococcus* sp. by Sumathi Rajasekharan.
Research supervisor: C. S. Vaidyanathan.
Department: Biochemistry.

1. Introduction

Microorganisms play a pivotal role in the biodegradation of many toxic and recalcitrant aromatic compounds, the accumulation of which in the soil would lead to ecological imbalance. Two major problems that render these compounds resistant to natural detoxification are their hydrophobic nature and toxicity. Microorganisms remarkably adapt themselves on these compounds and degrade them by enzymatic hydroxylation, thus making these compounds more soluble and less toxic. This aids in their further degradation.

The ability to hydroxylate aromatic rings is mostly confined to a group of enzymes which activate and reduce molecular oxygen with the help of prosthetic groups such as FAD, pteridine or metal ions[1].

A class of hydroxybenzoates, namely, 2-, 3- and 4-hydroxybenzoates are monohydroxylated mostly at position *ortho* to the existing hydroxyl group by flavin-containing external monooxygenases. Most of the studies on these flavoenzymes have been confined to gram-negative bacteria, namely, pseudomonads. However, much remains to be explored concerning the reaction mechanism of these enzymes in gram-positive bacteria.

A gram-positive bacterium, identified as *Micrococcus* sp., was isolated by soil-enrichment techniques. The organism was found to be degrading 3-hydroxybenzoate through hydroxylation at 6th position to yield gentisate; this pathway is uncommon among bacteria. The flavoenzyme, 3-HBA-6-hydroxylase catalysing this reaction is unique, that is, it introduces the incoming hydroxyl group at a position *para* to the existing group unlike other flavin monoxygenases. The flavenzyme has been reported only in *Pseudomonas* sp. and very little is known about its reaction mechanism. These considerations prompted the present investigation which was aimed at studying the chemistry of action of 3-HBA-6-hydroxylase in *Micrococcus* sp.

2. Results and conclusions

The enzyme was purified to homogeneity by employing Blue Sepharose affinity chromatography. The purification procedure revealed the formation of a ternary complex from the enzyme, 3-HBA and Blue Sepharose. The steady-state kinetics and physico-chemical properties of the purified enzyme were examined. The enzyme had an M_r of 70,000 without subunit structures and was distinctly different from the isofunctional enzymes isolated from *P. aeruginosa* and *P. cepacia*[2]. The prosthetic group of the enzyme was identified as FAD from the absorption and fluorescence spectra. The purified flavoenzyme catalysed a typical monooxygenation reaction which probably involved the sequential addition of 3-HBA, NADH and molecular oxygen in that order, to yield the product, gentisate. The uv-absorption and fluorescence spectra of the enzyme were typical of a protein containing tryptophan residues. The far-uv CD spectrum of the enzyme showed that the enzyme had α-helical secondary structure.

Fluorescence of tryptophan in a protein is highly sensitive to changes in the microenvironment[3]. A combination of results obtained from the studies on activity, fluorescence and circular dichroic properties of the enzyme in the presence of denaturants such as urea, guanidinium hydrochloride or SDS pointed out that the effect of these denaturants is localised and very subtle conformational changes in the environment of tryptophan residue(s), which is located at or near the active site of the enzyme, is responsible for the inactivation of the enzyme.

Chemical modification studies[4] suggested the probable involvement of arginine, histidine, cysteine and tryptophan residues in the activity of the enzyme. Physico-chemical studies on the modified enzyme indicated that the above-mentioned amino-acid residues are in close vicinity to each other and act in a concerted manner in the binding of 3-HBA.

A detailed physico-chemical investigation on the formation of a reversible complex between the oxidised flavoenzyme and substrate under varying conditions was undertaken. A wide variety of kinetic and physical probes are available to monitor the conformational changes and include various types of spectroscopy[5]. Fluorescence and CD spectroscopic studies indicated the participation of various non-covalent interactions such as electrostatic, hydrogen bonding and charge transfer in the stabilisation of ES-complex.

The mode of interaction of the enzyme with Cibacron Blue was studied since the dye specifically interacts at nucleotide-binding sites of enzymes such as dehydrogenases and kinases[6] and as it was used as an affinity ligand for purification of the flavoprotein. The catalytic activity of the enzyme is significantly inhibited by Cibacron Blue. Kinetic studies showed that the dye competes with NADH probably for the same site on the enzyme. At concentrations below 0·5 μM, the dye behaved as an uncompetitive inhibitor with respect to 3-HBA. A noncompetitive inhibition is observed at excess concentrations of dye which is due to the simultaneous formation of EI and ESI complexes. Equilibrium studies, *e.g.*, quenching of intrinsic fluorescence and perturbation of the near-uv CD spectrum of the enzyme by the dye indicate a change in the environment of tryptophan residue(s) of the enzyme which is either due to stacking of the indole ring of tryptophan upon Cibacron Blue or subtle conformational changes in the enzyme. The reduction in the association constant for the binding of dye to partially denatured (1M urea) enzyme emphasised the role of hydrogen bonds in the formation of enzyme-dye complex. All these studies indicate that Cibacron Blue is a valuable probe for examining the structure–function relationship in this enzyme.

References

1. Hayaishi, O., Katagiri, M. and Rothberg, S.	Mechanism of the pyrocatechase reaction, *J Am Chem Soc.*, 1955, **77**, 5450–5451.
2. Wang, L-H., Hamzah, R. Y , Yu, Y. and Tu, S. G.	*Pseudomonas cepacia* 3-Hydroxybenzoate 6-hydroxylase: induction, purification and characterization, *Biochemistry*, 1987, **26**, 1099–1104.
3. Herskovits, T T.	Difference spectroscopy, *Methods Enzymol.*, 1967, **11**, 748–775
4. Means, G. E. and Feeney, R. E.	*Chemical modification of proteins*, 1971, Holden-Day.
5. Citri, N.	Conformational adaptability in enzymes, *Adv. Enzymol.*, 1973, 37, 397–648.
6. Thompson, S. T., Cass, K. H. and Stellwagen, E.	Blue dextran–Sepharose–An affinity column for the dinucleotide fold in protein, *Proc. Natn. Acad. Sci.*, 1975, **72**, 669–672.

Thesis Abstract (Ph.D.)

Synthesis, spectra and structure of hydrazinium metal chloride and thiocyanate complexes by N. R. Sreenivasa Kumar.
Research supervisor: K. C. Patil.
Department: Inorganic and Physical Chemistry.

1. Introduction

Coordination compounds containing positively charged ligands are rare, in marked contrast to neutral and negatively charged ligands, and are of interest. The presence of positive charge in the vicinity of a potential donor atom in a cationic ligand does not prevent coordination to appropriate metal ion, even though the basicity is markedly lowered. In general, the effect of positive charge on the basicity of a donor atom depends upon their electronic interaction and their bonded distance within the ligand. Monoprotonated hydrazine, the hydrazinium cation ($N_2H_5^+$) stands unique among the known cationic polyamine ligands as the site of positive charge is immediately adjacent to the N-donor atom. Although the hydrazinium cation is a potential monodentate ligand[1–3], in some of the compounds it occurs as an uncoordinated cation[4–6]. From the literature survey, it is seen that although exhaustive amount of work has been done on hydrazinium metal sulphates, oxalates and hydrazinecarboxylates, very little is known about hydrazinium metal halides (with an exception of hydrazinium metal flourides) and pseudohalides. The present work aims at synthesis, characterization and thermal properties of hydrazinium metal chloride and thiocyanate complexes and also a study of the nature of coordination of $N_2H_5^+$ ion to various metal ions using spectroscopic and x-ray crystallographic studies.

2. Experimental

The complexes were prepared by the following methods:

(a) From the aqueous saturated solutions of the metal chlorides and $N_2H_4 \cdot HCl/N_2H_4 \cdot 2HCl$.

e.g., $(N_2H_5)_2\ MCl_4 \cdot 2H_2O$, M = Fe, Co, Ni, Cu, Pd and Pt; $(N_2H_5)\ ZnCl_4$ and $(N_2H_5)_3\ MnCl_5$.

(b) By decomposing the respective solid metal hydrazinecarboxylate complexes in the corresponding dilute acids.

e.g., $(N_2H_5)_2MX_4 \cdot 2H_2O$, M = Co and Ni, X = Cl and SCN; $(N_2H_5)_2ZnCl_4$;$(N_2H_5)MBr_4 \cdot 4H_2O$, M = Co and Ni; $(N_2H_5)\ MnX_5$, X = Cl and Br.

(c) By refluxing iron (III) chloride and $N_2H_4 \cdot HCl$ in ethanol.

e.g., $(N_2H_5)_4\ FeCl_6$.

All the complexes were characterized by conventional chemical analysis, spectral and other techniques which include thermal analysis (TG and DTA), infrared, electronic and Mossbauer spectra, magnetic susceptibility measurements and single-crystal x-ray diffraction studies.

3. Main results

Hydrazinium metal chloride hydrates, $(N_2H_5)MCl_4 \cdot 2H_2O$ where M = Fe, Co, Ni, Cu, Pd and Pt exhibit a sharp ir absorption band in the region 995–1020 cm^{-1} corresponding to the N–N stretching frequency of $N_2H_5^+$. This is a clear indication of coordination of ions to the metal[7]. The coordination of $N_2H_5^+$ ion to metal has been confirmed by single-crystal x-ray diffraction studies.

The crystal structure of iron complex, $(N_2H_5)_2\ FeCl_4 \cdot 2H_2O$ clearly showed the coordination of $N_2H_5^+$ ions to metal. In the crystal the iron atom has octahedral coordination and is bonded by two hydrazinium cations, two water molecules and two chlorines through *trans* positions. Preliminary studies on the single crystals of cobalt complex showed that the molecule has an inversion centre, implying that the bonded groups are *trans* to each other. From spectral data, similar structure has been assigned to the nickel complex.

Structure of the platinum complex $(N_2H_5)_2PtCl_4 \cdot 2H_2O$ shows that the metal has square planar configuration, coordinated by two hydrazinium cations and two chloride ions through *trans* positions. The observed *trans* structure is contradictory to the expected *cis* structure and from spectral studies, the formation of *trans* complex has been ascribed to reduced repulsion between the two $N_2H_5^+$ ions in *trans* structure compared to the *cis* one. Palladium complex is expected to have the same structure. Infrared spectral data indicated that the bromide complexes, $(N_2H_5)_2MBr_4 \cdot 4H_2O$ (M = Co and Ni) have coordinated $N_2H_5^+$ ions.

In $N_2H_5CuCl_3$ and $(N_2H_5)_2ZnCl_4$, all the $N_2H_5^+$ ions present in the complexes are coordinated to the metals whereas in manganese complex, $(N_2H_5)_3MnCl_5$, only one of the three $N_2H_5^+$ ions is coordinated to the metal. Crystal structure of this complex shows octahedral geometry around manganese atom. The bromide complex, $(N_2H_5)_3MnBr_5$, shows similar characteristics in spectral properties as that of chloride and hence similar structure has been assigned to it.

Hydrazinium metal thiocyanate complexes of cobalt and nickel have been prepared for the first time. Structure of $(N_2H_5)_2Co(NCS)_4 \cdot 2H_2O$ shows that the metal is six coordinated by two $N_2H_5^+$ ions in *cis* positions and by four –NCS groups. Two of the –NCS groups have linear metal–NCS linkages and the other two have angular metal–NCS linkages. Preliminary data obtained from the single crystals of $(N_2H_5)_2Ni(NCS)_4 \cdot 2H_2O$ show that the complex is isostructural with the cobalt complex.

A nickel thiosemicarbazide complex, $Ni(N_2H_3 \cdot CS \cdot NH_2)_2(NCS)_2$ has been isolated during the preparation of $(N_2H_5)_2Ni(NCS)_4 \cdot 2H_2O$. This is due to the rearrangement of hydrazinium thiocyanate to thiosemicarbazide. The structure of the thiosemicarbazide complex has been determined and shown that the nickel atom is coordinated by two bidentate thiosemicarbazide molecules and by two N-bonded thiocyanates.

4. Conclusions

(i) All the complexes have coordinated $N_2H_5^+$ ion(s) and in all the complexes, the hydrazinium cation forms weak metal–nitrogen bond, platinum being an exception.

(ii) The N–N bond lengths in all the complexes are near 1·44Å, in between the values of N_2H_4 and $N_2H_6^{2+}$.

(iii) There is no significant change in the N–N bond length of $N_2H_5^+$ upon coordination.

(iv) It appears that the maximum number of $N_2H_5^+$ ions a metal can accommodate in its coordination sphere may not exceed two.

(v) Hydrazinium cations are in *trans* positions in all chloride and bromide complexes whereas they are in *cis* positions in thiocyanate complexes.

(vi) Thermal analysis of all the complexes shows loss of hydrazine at relatively higher temperatures in accordance with the structure.

References

1. Prout, C K and Powell, H. M — *J. Chem Soc.*, 1961, 4177–4182.
2. Govindarajan, S , Patil, K C. Manohar, H M and Werner, P. E — *J Chem. Soc. Dalton Trans.*, 1986, 119–123
3. Brown, D B , Donner, J. A , Hall, J. W., Wilson, S. R., Wilson, R B., Hodgson, D J and Hatfield, W. E. — *Inorg. Chem.*, 1979, **18**, 2635–2641.
4. Poojary, M D. and Patil, K. C — *Proc Indian Acad. Sci. (Chem Sci.)*, 1987, **99**, 311–315
5. Gajapathy, D , Govindarajan, S., Patil, K. C. and Manohar, H. — *Polyhedron*, 1983, **2**, 865–873.
6. Govindarajan, S , Patil, K C , Poojary, M D. and Manohar, H. — *Inorg. Chim Acta*, 1986, **120**, 103–107.
7. Braibanti, A , Dallavalle, F., Pellinghelli, M A. and Laporati, E. — *Inorg. Chem.*, 1968, 7, 1430–1433.

Thesis Abstract (Ph.D.)

Synthesis and reaction of oxygen and nitrogen heterocycles by Lata Mathew.
Research supervisor: T. R. Kasturi.
Department: Organic Chemistry.

1. Introduction

Synthesis of heterocyclic compounds which are of biological importance like Olivacine and water-soluble 1,2-dihydroisoquinolines was envisaged. Working in this field led us to a novel heterocyclic ring system, namely, benzo [de] [2,7] naphthyridine *via* Vilsmeier–Haack reaction of 5,6,7,8-tetrahydroisoquinolines and also *in-situ* alkylations of 5,6-dihydroisoquinolines *via* potassamide in liquid ammonia reaction. We also investigated the mechanism of the reaction leading to these products.

2. Results and discussion

Synthesis of spironaphthalenones (1b) and (1c) was achieved starting from *m*-cresol methyl ether by

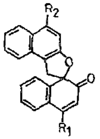

1a $R_1 = R_2 = H$
b. $R_1 = CH_3$; $R_2 = H$
c. $R_1 = H$; $R_2 = CH_3$

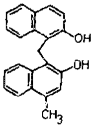

2

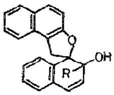

3a $R = H$
b. $R = CH_3$
c. $R = Ph$

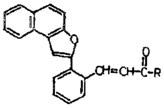

4a $R = H$
b. $R = CH_3$
c. $R = Ph$

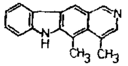

5

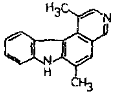

6

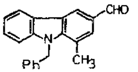

7

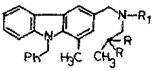

8a. $R_1 = H$; $R = OCH_3$
b $R_1 = Ts$, $R = OCH_3$
c. $R_1 = Ts$; $\overset{R}{\underset{R}{>}}=O$

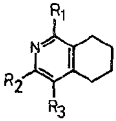

9a. $R_1 = R_2 = OCH_3$; $R_3 = CN$
b. $R_1 = R_2 = OH$; $R_3 = CN$
c. $R_1 = R_2 = OH$; $R_3 = H$
d. $R_1 = R_2 = OCH_3$; $R_3 = H$
e. $R_1 = R_2 = OCH_3$; $R_3 = CHO$
f. $R_1 = Cl$; $R_2 = OCH_3$; $R_3 = CHO$
g. $R_1 = OCH_3$; $R_2 = Cl$; $R_3 = CHO$

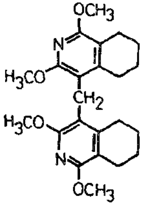

10

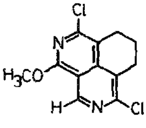

11

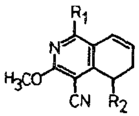

12a. $R_1 = CH_3$; $R_2 = H$
b. $R_1 = Et$; $R_2 = H$
c. $R_1 = CH_3$; $R_2 = CH_3$
d. $R_1 = Et$; $R_2 = CH_3$

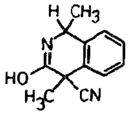

13

succinoylation, Clemmensen reduction, cyclisation, borohydride reduction, dehydration and aromatisation followed by demethylation to obtain 4-methyl-2-naphthol. This was condensed with the sodium salt of 2-naphthol-1-methyl sulphonic acid to give (2). Pottassium ferricyanide oxidation of (2) gave the required spironaphthalenone (1b) and (1c). Sodium borohydride reduction of the spironaphthalenone (1a) gave the allylic alcohol (3a). DDQ oxidation of (3a) in benzene resulted in transformation to a mixture of *cis*- and *trans*-α, β-unsaturated aldehyde (4a). Grignard reaction of (1a) with methylmagnesium iodide and phenylmagnesium bromide gave the allylic alcohols (3b) and (3c), respectively, the unsaturated ketones (4b) and (4c) as *cis*- and *trans*-isomers.

Synthesis of isomers (5) and (6) of Olivacine was attempted by the method of Murakami *et al* [1]. The starting aldehyde (7) was prepared from N-benzyl tetrahydrocarbazole by Vilsmeier reaction. Reaction of this aldehyde (7) with aminoacetone dimethyl ketal followed by borohydride reduction gave the amine (8a). Tosylation with *p*-toluenesulphonyl chloride in triethylamine resulted in the formation of the corresponding tosylate (8b). Mild acid hydrolysis of (8b) gave the tosyl ketone (8c). However, treatment of the ketone (8c) with HCl–dioxan or P_2O_5–benzene did not result in cyclisation but gave the cleaved N-tosyl aminoacetone.

Vilsmeier reaction of 5,6,7,8-tetrahydroisoquinoline (9a) gave three compounds identified as (9d), (9e), and (10) based on spectral data[2]. Plausible mechanisms for the formation of these compounds have been suggested. Vilsmeier reaction of the corresponding dihydroxy compound (9b), followed by methylation, however, resulted in the formation of two distinct compounds for which structures (9f) and (11) have been proposed, based on a detailed study of their spectral characteristics. Vilsmeier reaction of (9c) followed by methylation was found to give (9g). Nuclear Overhauser studies ruled out alternative structures for these compounds.

Potassamide in liquid ammonia reaction of 5,6-dihydroisoquinolines was reported to give 1,2-dihydroisoquinolines and isoquinolines[3] The reaction of (12a) and (12b) followed by *in-situ* alkylation with alkyl halides was studied. Thus, reaction of (12a) with KNH_2 in liquid ammonia followed by addition of methyl iodide *in situ* gave rise to C-alkylated 5,6-dihydroisoquinolines (12c) and (12d) and another dihydroisoquinoline (13). Alkylation of (12b) by potassamide reaction with alkyl halides (CH_3I and C_2H_5I) gave similar products.

References

1 Murakami, Y. Yokoyama, Y. and Okuyama, N. — The Vilsmeier–Haack reaction of N-alkyl-1,2,3,4-tetrahydrocarbazoles and the synthetic application to Olivacine and ellipticine, *Tetrahedron Lett.*, 1983, **24**, 2189–2192.

2 Kasturi, T. R., Jois, H. R. Y. and Lata Mathew — A novel transformation of 3-alkoxyisoquinolines to 3-chloroisoquinolines and an unusual decyanation of 1,3-dialkoxy-4-cyano-5,6,7,8-tetrahydroisoquinolines under Vilsmeir–Haack conditions, *Synthesis*, 1984, 743–746.

3. Kasturi, T. R., Lalitha Krishnan and Prasad, R. S. — Amide-catalysed isomerization of 5,6-dihydroisoquinolines: a novel synthesis of 1,2-dihydroisoquinolines, *J. Chem. Soc. Perkin Trans. I*, 1982, 63–68

Thesis Abstract (Ph.D.)

Cosmological singularity, torsion and creation field by Ramanand Jha.
Research supervisor: K. P. Sinha.
Department: Physics.

1. Introduction

The hot big-bang cosmology (BBC) based on Einstein's general theory of relativity (GTR) nicely accounts for the universal Hubble expansion, the T=2·7K cosmic microwave background radiation, and, through primordial nucleosynthesis, the abundances of ^{4}He, ^{2}H, and perhaps also ^{3}He and ^{7}Li. However, the hot BBC by itself fails to account for a number of fundamental cosmological facts. They include: the large-scale homogeneity and isotropy of the universe, the origin of small-scale inhomogeneity, the flatness of the universe today, the predominance of matter over antimatter, the absence of topological defects (*e.g.*, magnetic monopoles, domain walls, etc.), and the extreme smallness of the present value of the cosmological constant. There have been many modifications to Einstein's equations but none of them is capable of solving all the difficulties encountered in GTR.

2. Formulation of the problem

Of the numerous theories of gravity that have been proposed as modifications to Einstein's theory of gravitation, one of the most long-lived has been the ECSK theory (a U_4-theory of gravitation) which allows for a non-zero torsion tensor.

The various aspects of the work have been the exploration of the possible role of scalar fields in gravitational theories in Riemannian and non-Riemannian manifolds. There are two distinct ways in which a scalar field can have a non-trivial effect when introduced into a gravitational theory:

1. By being coupled nonlinear to the gravitational field as in the Brans–Dicke theory or the conformal-type coupling.
2. By appealing as a negative energy field, *e.g.*, creation field

One can also consider a scalar field that satisfies both these conditions.

3. Results and conclusions

Many interesting and surprising results have been obtained in this work. It includes generation of torsion in space–time from a scalar field, in contrast to standard ECSK theory where torsion is generated through the spin of the elementry particle[1]; the consequence of the Brans–Dicke (BD) theory in the U_4-manifold is indistinguishable from the BD theory in Riemannian manifold in the solar system experiments[2]; a conformal scalar field along with gravitation in U_4-manifold leads to a singularity-free cosmological model (it is the singularity of cosmological models which is responsible for many cosmological problems). It has also been shown that a negative energy massive scalar field minimally coupled to gravity naturally leads to a potential which is capable of explaining the small anomalous effect in the Eötvös experiment[3] (which led to the hypothesis of a controversial fifth force). Finally, the famous Hoyle–Narlikar creation theory[4] has been modified in such a way that the new theory is complete, in contrast to the former theory where the rate of creation has to be specified in an arbitrary manner.

References

1. Hehl, F. W., von der Heyde, P. Kerlick, G. D. and Nester, J. M.	General relativity with spin and torsion: Foundations and prospects, *Rev Mod Phys*, 1976, **48**, 393–416.
2. Brans, C. and Dicke, R. H.	Mach's principle and a relativistic theory of gravitation, *Phy. Rev.*, 1961, **124**, 925–935.
3. Fischbach, E., Sudarsky, D., Szafer, A., Talmadge, C. and Aronson, S. H.	Reanalysis of the Eotvos experiment, *Phys. Rev Lett.*, 1986, **56**, 3–6.
4. Hoyle, F. and Narlikar, J. V.	Mach's principle and the creation of matter, *Proc. R. Soc. Lond A*, 1963, **273**, 1–11

Thesis Abstract (Ph.D.)

NMR spectroscopy of oriented systems: studies at and near magic angle sample spinning

by B. S. Arun Kumar.
Research supervisors: K. V. Ramanathan and Anil Kumar.
Department: Physics.

1. Introduction

In contrast to molecules dissolved in isotropic liquids in which many of the inter- and intra-molecular interactions get averaged to their isotropic value, molecules oriented in liquid crystals retain partially the anisotropy of the interactions due to restricted motions. In the study of oriented molecules by nuclear magnetic resonance (nmr), this property is taken advantage of. For molecules oriented in nematic liquid crystals, inter-molecular interactions of relevance to nmr are averaged to zero, but the intra-molecular interactions are only partially averaged. This apparent advantage also increases the complexity of the nmr spectrum. Hence in practice only systems with a limited number of interacting nuclei could be studied. It was shown that by spinning the sample close to 'magic angle' all anisotropic interactions are scaled down by a factor $(3\cos^2\Theta - 1)/2$ where Θ is the angle between the magnetic field and the spinning axis, thereby simplifying the spectrum[1]. In this work, the effect of magic angle and near-magic angle spinning on the director is studied in such systems as single liquid crystals, mixed liquid crystals of opposite diamagnetic susceptibility anisotropy and lyotropic liquid crystals. A new method of setting the magic angle from the spectra of oriented molecules is proposed. The effect of the sign of the order parameter on the spinning side band intensities is discussed. Finally, ^{13}C chemical shift anisotropy of the liquid crystal carbons is determined from the 'coexistence'[2] spectra of two liquid crystals of opposite diamagnetic susceptibility anisotropies ($\Delta\chi$).

2. Director dynamics at 'near-magic angle sample spinning'

Complicated spectra of molecules oriented in liquid crystals can be simplified by spinning at or near-magic angle. For this purpose it is essential to understand the dynamics of the director and the resulting spectra under near-magic angle spinning conditions. It is found that when a mixture of liquid crystals of opposite diamagnetic susceptibility anisotropy with macroscopic $\Delta\chi$ is slightly positive spun at angles less than magic angle (54·7°), the director orientation switches at increasing spinning speeds from one that is parallel to the spinning axis to the one that is orthogonal to it. Similar results are obtained for systems with macroscopic $\Delta\chi$ slightly negative except that it is for angles greater than magic angle. This has been explained in terms of the interplay of the two torques, *viz.*, viscous and magnetic.

In the case of single liquid crystals under spinning conditions, it has been shown previously[1] that for a positive $\Delta\chi$ system the director orients parallel to the spinning axis for angles less than the magic angle, while for angles greater than magic angle it is distributed in a plane perpendicular to it and *vice versa* for a negative $\Delta\chi$ system. However, it is found that for angles other than magic angle, the director orientation deviates from the plane that is perpendicular to the spinning axis for lower spinning speeds. From the intensity of the spinning side bands, the distribution has been estimated. All of the above results have been obtained from ^2H nmr spectra of $CDCl_3$ oriented in liquid crystals ZLI-1167 ((a ternary eutectic mixture of propyl, pentyl and heptyl bicyclohexyl carbonitrile) and S-1114 (trans *p* pentyl–4 cyanophenyl)–cyclohexane).

3. Setting the magic angle from the spectra of oriented molecules

All anisotropic interactions in the case of oriented molecules are scaled by a factor $(3\cos^2\Theta - 1)/2$ on spinning. For magic-angle spinning all anisotropic interactions are reduced to zero. The ^{13}C spectrum of $CHCl_3$ oriented in a liquid crystal at magic angle consists of a doublet with the doublet separation equal to the scalar coupling between ^{13}C and ^1H. For other angles the doublet separation is different due to ^{13}C–^1H dipolar interaction. The magic angles can thus be accurately set using the spectra of oriented molecules.

4. Determination of the sign of the order parameter

In oriented systems the sign of the order parameter cannot be straightaway determined from the normal spectrum. Theoretical calculations are carried out to show that from the side band intensities of spinning oriented samples, the sign of the order parameter can be found under certain conditions. This is demonstrated using compounds such as $CHCl_3$ and C_6H_6 oriented in liquid crystals.

5. Determination of the chemical shift anisotropy of individual carbons of liquid crystals

The proton-decoupled ^{13}C nmr spectra of mixtures of liquid crystals with opposite diamagnetic anisotropies have been studied in the natural abundance of ^{13}C. A new method to assign the spectral lines to specific carbons in the liquid crystalline phase is given which requires the assignments of lines in the isotropic phase. These assignments are obtained from two-dimensional hetero COSY experiments. From the spectra in 'critical' mixtures where both the orientations of the liquid crystal directors, with the alignments along and perpendicular to the direction of the magnetic field, 'coexist', the ^{13}C chemical shift anisotropies have been determined assuming uniaxial symmetry.

References

1. Courtieu, J., Alderman, D. W., Grant, D M and Bayles, J. P. — *J. Chem. Phys*, 1982, **77**, 723–730.
2. Khetrapal, C. L. and Kunwar, A. C. — *Chem Phys. Lett.*, 1981, **82**, 170–171.

Thesis Abstract (Ph.D.)

The fluorescence of manganese in mixed sulphate glasses and crystalline medium by N. Manickam.

Research supervisors: C. K. Subramanian and P. S. Narayanan.
Department: Physics.

1. Introduction

When the ions of a transition metal element are introduced into glasses, they exhibit optical properties which are modified by the structure of glass matrix. These changes therefore can be used for probing the local coordination in the glasses. The spectral and temporal characteristics of a laser radiation enable a selective excitation of ions in the glasses. An investigation was therefore undertaken to study the local coordination of manganese ions in K_2SO_4–$ZnSO_4$ glass and measure the fluorescence decay time of the $^4T_{1g}$ state of the manganese ion. In particular an attempt was made to see the effect of glass composition and concentration of manganese on the fluorescence spectrum and decay time measurement in K_2SO_4–$ZnSO_4$ glass.

A study was also made to see the effect of phase transition on the fluorescence decay time of the manganese ions above and below the phase-transition temperature in the $K_2Mn_2(SO_4)_3$ crystal of the langbeinite family.

2. Experimental techniques

The pumping source used for the fluorescence decay time measurement was a nitrogen laser and nitrogen laser pumped dye laser fabricated in the laboratory for this purpose. The nitrogen laser was fabricated using a standard Blumlein voltage doubling circuit with a spark gap firing[1]. The plasma tube has an aluminium reflector at the back and a quartz output window in the front and was 100 cm long. Breakdown occurred between electrodes of circular crosssection separated by 1 cm. Peak power was obtained when the windows were aligned and the pressure inside the plasma tube was maintained at 90 Torr with a controlled flow of nitrogen gas. The total storage capacitance of the energy storage capacitor was 25·3 nF, and the spark gap was fired at 12 kV. The output ultraviolet (337·1 nm) laser pulse was 8 ns long with a peak power of about 200 kW at 10 Hz. The laser beam spot size at the output was rectangular measuring 10×5 mm^2.

This nitrogen laser was used to pump a dye laser. Grazing incidence grating–mirror combination was used to tune the dye laser output[2]. The optical cavity was defined by two fully reflecting aluminium mirrors and a Bausch and Lomb holographic grating 1200 lines per mm blazed at an angle of 17° 27″. Various organic dyes like Rhodamine 6G, Rhodamine B were made to lase. The dye laser pulse width was about 5 ns. The fluorescence from the glass sample, viewed at 90° relative to the incoming laser beam was collimated and focused with lenses on to the slit of a monochromator. The light reaching the exit slit of the monochromator was monitored with an EMI 9558 B photomultiplier tube which has an extended S–20 response. The output of the photomultiplier was fed to a digital storage (Iwatsu, DMS 6430) and the oscilloscope output was recorded by recorder (Phillips PM 8120). The oscilloscope was triggered by a photodiode (HP 4207) which sensed a fraction of dye laser beam.

Glass samples were prepared following the procedure of Narasimhan *et at*[3]. Analar-grade manganese sulphate was used in different concentrations for all the glass compositions prepared (3 to 12 mole per cent). Absorption and fluorescence spectra were recorded with Hitachi 557 model spectrophotometer and 770 model spectrofluorimeter, respectively. To record the fluorescence signal from the crystal at low temperature an optical cryostat was fabricated.

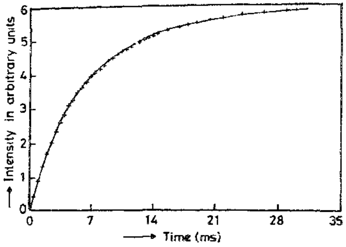

FIG. 1. Fluorescence decay of Mn(II) ion in sulphate glass (40 K_2SO_4: 57 $ZnSO_4$· 3 $MnSO_4$).

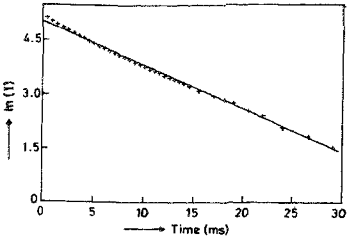

FIG. 2. Logarithmic plot of decay in Fig. 1.

3. Results

The absorption spectrum revealed that manganese has an octahedral coordination in K_2SO_4–$ZnSO_4$ glass. When the glass sample was excited with a wavelength corresponding to the peak of the absorption wavelength (407 nm), fluorescence was observed at 615nm for 3 mole per cent of manganese sulphate in K_2SO_4–$ZnSO_4$ glass which is characteristic of Mn^{2+} ion in octahedral coordination.

Fluorescence decay times of the radiation originating from $^4T_{1g}$ state and terminating in $^6A_1$ state in the wavelength range 615–630 nm have been measured at room temperature. For each decay curve the function ln(I) has been plotted against time. A typical ln(I) *vs* time(T) plot corresponding to the decay curve shown in Fig. 1. is given in Fig. 2. The slope of the straight line is a measure of the fluorescence decay time. The plots were found to be in straight line in all cases showing that the fluorescence decay times were a single exponential. The decay times became shorter as the concentration of manganese is increased for a given composition of K_2SO_4–$ZnSO_4$ glass. This decrease is attributed to the concentration quenching by

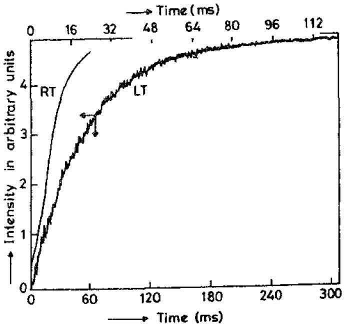

FIG. 3. Fluorescence decay of Mn(II) ion in $K_2Mn_2(SO_4)_3$ crystal (RT: room temperature: and LT: low temperature (100 K)).

manganese ion–ion interaction. The decay times also decreased as monovalent ions like lithium and sodium were substituted for potassium for a given concentration of manganese. This dependence of decay time is due to an increase in the radius of monovalent ions.

Fluorescence decay time of manganese in potassium manganese sulphate crystal [$K_2Mn_2(SO_4)_3$] showed a marked change from 0·8 ms at room temperature to 30 ms at low temperature (100 K). The decay curve of the red fluorescence recorded at room temperature and at low temperatures (100 K) is shown in Fig. 3. The increase in decay time is due to decrease in vibrational energy at lower temperature. This can therefore be a useful technique which could be used to investigate structural phase transitions.

References

1. Basting, D., Schafer, F. P. and Steyer, B.	*Opto-Electronics*, 1972, **4**, 43–44.
2. Shoshan, I., Danon, N. N. and Oppenheim, V. P	*J. Appl. Phys*, 1977, **48**, 4495–4497.
3. Narasimham, P. S. L. and Rao, K. J	*J Noncrystalline Solids*, 1978, **27**, 225–246

Thesis Abstract (Ph.D.)

Studies on cryogenic multilayer insulations and the development of cryogenic containers

by Subhash Jacob.
Research supervisors: E. S. Raja Gopal and P. S. Narayanan.
Department: Physics.

1. Introduction

Multilayer insulation (MLI) is the most efficient cryogenic insulation available currently. In general, a large number of highly reflecting shields interposed by thermal spacers are placed in a high vacuum environment to form multilayer insulation. This work deals with the heat transfer and allied studies of MLI (300–77K) and the design and development of multilayer-insulated cryogenic containers.

2. Experimental programme and results

2.1. *Calorimetric studies*

Calorimetric investigations have been carried out on MLI using three specially designed calorimeters: (a) a double-guarded cylindrical calorimeter, (b) a tank calorimeter, and (c) a flat-plate calorimeter. The first two have been designed for heat-transfer studies whereas the flat-plate calorimeter is for interlayer gas-pressure measurements in MLI. Indigenous double-sided aluminized Mylar (DAM) and thin nylon net have been used as radiation shields and thermal spacers, respectively.

Heat-transfer measurements have established that the optimum number of layers of the indigenous materials in the MLI is 40–50 layers, at a layer density of 25 layers per cm, to obtain minimum heat flux and effective thermal conductivity. The optimum effective thermal conductivity (K_{eff}) values of the MLI samples have been about 0·9 μW/cm K. Critical dependence of the heat flux, steady-state temperature profile of the MLI and cooldown time on the insulation chamber pressure have been studied. The temperature profile of the insulation provides an indication as to the predominance of the radiative or conductive heat-transfer component for the MLI system under specific experimental conditions. For the same number of layers, the temperature of any specific layer within the boundaries decreases with the increase in the chamber pressure. At the same time, the heat flux through MLI increases and is more critical for MLI with fewer number of layers. The degradation factor in the K_{eff} of the MLI for actual application as compared to idealised conditions has been estimated as 1·68.

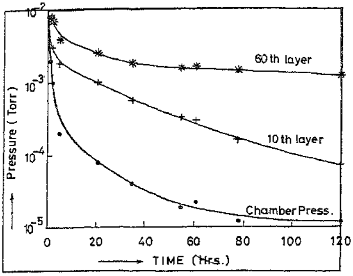

FIG. 1 Interlayer gas pressure (Isothermal test 300 K)

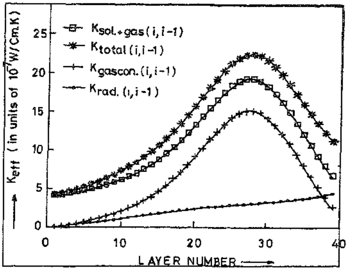

FIG 2 Sectional effective thermal conductivity components of MLI (Chamber pressure = 5E-T Torr and number of layers, $n = 39$.

Interlayer gas pressures in MLI have been measured at ambient and low temperature conditions of the sample using a flat-plate calorimeter. Studies establish higher interlayer gas pressure at the middle zones of the sample (Fig. 1). The pressure distribution appears to be highly influenced by the pressure of mobile water molecules within the insulation.

2.2. *Heat-transfer models and analysis*

Heat-transfer analysis of calorimetric investigations has been carried out using different analytical models[1,2]. K_{eff} components of different sections of the insualtion have been computed. A typical K_{eff} sectional analysis is shown in Fig. 2. Sectional analysis shows a peak for K_{eff} in between the middle and the warm boundary region which is primarily due to higher residual gas conduction at this section. Theoretical estimation of heat flux for different number of MLI layers at high and low vacuum conditions has been obtained using a heat-transfer model accounting for nonlinear temperature profile in MLI. A comparison of the theoretical and experimental heat fluxes shows that, in general, the theoretical model predicts a lower heat flux. This can be attributed to the assumption of negligible residual gas conduction in model analysis. A new model has been suggested which accounts for the temperature and spatial dependence of the interlayer gas pressure. Transient heat-transfer analysis has been carried out using a one-dimensional model for typical experimental cases. Thermal diffusivities of MLI samples have been estimated from the above analysis as about 10^{-9} m^2 s^{-1}

2.3. *Material characterisation studies*

Some characterisation studies of insulation and other materials used in cryogenic containers have been carried out as part of the work Outgassing rates of samples have been estimated and residual gas studies have been carried out using a quadrupole mass spectrometer. The studies have established that water is the main species of outgassing from the samples and specific preconditioning with vacuum-desorption under heating is needed to qualify them for cryogenic applications.

2.4. *Studies and development of liquid nitrogen containers*

Studies have been carried out related to the development of 30 l capacity liquid nitrogen containers. A modified low-temperature adhesive has been developed[3] and its low-temperature shear strength is determined to be about 6·27 MN/m^2. Free atmospheric adsorption studies have been carried out on activated charcoal and zeolite 5A. Zeolite 5A showed a 20 per cent increase in weight when it got saturated while the saturation percentage was between 11 and 6·5 per cent in the case of activated charcoal. A heat-transfer separation into radiative and conductive components has been obtained for the liquid nitrogen container by varying its outer boundary temperature[4].

2.5 Studies and development of mobile liquid oxygen tank

A 220 l capacity liquid oxygen tank has been developed. It has been built for charging liquid oxygen to breather converters of fighter aircraft. A unique support mechanism has been developed to take care of high acceleration loads and thermal contraction effects. A novel method of using the non-evaporable getter Zr–Ve–Fe as an *in-situ* appendage pump has shown that the insulation vacuum level can be maintained by the getter. Cryogen transfer studies have shown that the transfer efficiencies decrease with decrease in the liquid level for the horizontal tank. This has been attributed to a complex interaction of the effects due to stratification, dissipation energy due to flow losses and external heat leak to transfer pipeline.

References

1. Verkin, B. I , Mikhalchenko, R. S and Gerzhin, A. G	Effect of multilayer insulation on apparent thermal conductivity, *Proc. ICEC-2,* Brighton, UK, 1968, pp 123–127
2. Inai, N	Recent advances in the investigation of multilayer insualtion, *Trans. JSME,* 1977, **43**, 217–224
3. Jacob, S., Karunanithi, R., Kasthurirengan, S., and Manjunath, G.	Development and application of a modified low temperature epoxy adhesive, *Proc ICEC-12,* Southampton, UK, 1988, pp 442–445.
4. Kutzner, K., Schmidt, F. and Wietzke, I.	Radiative and conductive heat transmission through superinsulations—experimental results for aluminium-coated plastic foils, *Cryogenics,* 1973, **13**, 396–404

Thesis Abstract (Ph.D.)

Experimental studies on sound propagation in shallow waters off the west coast of India by O. Vijayakumar.

Research supervisors: E. S. R. Gopal and V. K. Aatre (NPOL, Cochin).
Department: Physics.

1. Introduction

Underwater acoustics has acquired a degree of importance in applied physics. The present work is devoted to an experimental study on sound propagation in the shallow water region off the west coast of India. This study may be considered as the first of its kind carried out in the Indian coastal waters. In the present study, transmission loss (TL) is measured and its behaviour is correlated with the corresponding environmental variations. The frequency dependence of TL is studied in detail and the existence of an optimum frequency of propagation is highlighted. An analytical model based on normal mode theory is also developed and compared with experimental observations.

2. Experimental observations

The experiments were conducted at four different shallow-water regions of west coast of India[1]. Two ships, one as transmitting and the other as receiving, were used in these experiments. Underwater explosives provided wideband sound sources[2]. The receiving ship was anchored and deployed an array of hydrophones. It carried recording equipment. The transmitting ship which carried the explosives opened out from the receiving ship along a prescribed constant depth track deploying explosives at different ranges. The signals received were recorded on an analog magnetic tape recorder and later analysed in the laboratory. The parameter estimated was TL and the estimation scheme was tailored to suit an easy comparison with model predictions. We estimated 1/3 octave averaged TL values so that they could be compared with model predictions obtained by an incoherent summation of normal modes.

3. The normal mode acoustic propagation (NAP) model

The acoustic conditions of many of the shallow-water areas may be approximated to the so-called Pekeris

Channel[3], that is, a layer of isospeed water overlying a homogeneous isospeed, semi-infinite sediment bottom. This approximation is good in many cases and there exists vast shallow-water areas with homogeneous sediment bottoms. The approximation of isospeed water layer holds good at low frequencies. Using these approximations, an analytical model based on normal mode theory is developed.

The present model[4] is essentially based on the normal mode theory for the Pekeris Channel. However, all the important losses occurring in the medium are incorporated in order to provide a realistic estimate of TL. The model has got various options such as computing the coherent and incoherent transmission losses[5], different types of averaging and providing different types of plots. The computation of group velocities of normal modes is provided as an additional option.

4. Data/ model comparisons—Discussion and results

The experimental data averaged over 1/3 octave frequency bands provide a stable comparison with the theoretical values computed by the incoherent addition of normal modes[6]. Further, the use of certain averaging schemes are also justified in the light of the acoustic pressure fluctuations related to medium disturbances. Two types of averagings are employed, namely, frequency averaging over 1/3 octave bands and depth averaging over many receiver depths. Depth averaging is particularly useful in studying in variation of TL with range and frequency. For these particular applications, a measure of energy flux over the water column rather than the field at a specific depth is required.

The data/model comparisons show a fairly good agreement over the mid-frequency region of 100–1000 Hz. The predictions are not very good at very low and high frequency regions since many details such as the sound speed profile of water column, layering of the sea bottom, sound speed gradients in various sea bottom layers and the roughness of the sea bottom are not included in the model. Even if all the above-mentioned details are included to make a complex model, reliable predictions become difficult, unless detailed data of the sea bottom are available. Presently such data are not available for our shallow water areas. In the absence of such data, what an acoustician can do is to use the data/model comparisons to arrive at the relevant sea bottom parameters by the method of 'fine-tuning'. The values obtained by fine-tuning method provide more reliable data for acoustical prediction purposes.

5. Optimum frequency of propagation

The frequency response of shallow water sound propagation is 'band pass' in nature which is characteristic of any type of guided wave propagation. There exists a frequency band which suffers minimum TL. The optimum frequency[7,8] depends mainly on the water depth and sea bottom type. In the present study, three typical experimental results are discussed and compared with model predictions. It is found that for simple shallow-water channels with isovelocity water overlying a homogeneous sediment bottom, the optimum frequency could be predicted with relative ease. The problem becomes complex when the bottom is layered[9]. Such a case is also presented where the experimental results showed an optimum frequency which is far below the value predicted by the present model. The reason is attributed to a presumed layered structure of the bottom and the existence of a thin low-speed sediment layer.

References

1. Vijayakuamr, O. and Abdul Salam, K. A.	*Shallow water sound propagation off Bombay,* Report No. RR-10/85, NPOL, Cochin, 1985.
2. Weston, D. E.	Underwater explosions as acoustic sources, *Proc. Phys. Soc.* (Lond.), 1960, **76**, 233–249.
3. Pekeris, C. L.	Theory of propagation of explosive sound in shallow water, *Geol Soc. Am. Mem.*, 1948, 27.
4. Vijayakumar, O. and Ajaikumar, M. P.	A normal mode analytical model for sound propagation in shallow waters and comparison with experimental data, Report No. RR-8/89, NPOL, Cochin, 1989.
5. Jensen, F. B. and Ferla, M. C.	*SNAP: The saclntcen normal mode acoustic propagation model,* Saclntcen memorandum, SM–121, Jan. 1979.

6. Ferla, M. G , Drenini, G , Jensen, F. B. and Kuperman, W A. Broadband model/data—Comparisons for acoustic propagation in coastal waters, *Bottom interacting ocean acoustics,* 1980, Plenum.

7. Jenson, F B. and Kuperman, W. A Opimum frequency of propagation in shallow water environments, *J. Acoust. Soc. Am.*, 1983, **79**, 813–819

8. Eller, A. I. and Gershfeld, D A. Low-frequency acoustic response of shallow water ducts, *J. Acoust. Soc. Am.*, 1985, **78**, 622–631.

9. Rubano, L A. Acoustic propagation in shallow water over a low-velocity bottom, *J. Acoust. Soc Am.*, 1980, **67**, 1608–1613.

Thesis Abstract (M.Sc. (Engng))

Bubble formation in moving foams by Sushma R. Nair.
Research supervisors: R. Kumar and K. S. Gandhi.
Department: Chemical Engineering.

1. Introduction

Liquid membranes offer an interesting method of separation which has recently been commercially employed for zinc recovery from an effluent stream. It has also been shown on the laboratory scale that the same concept can be used for enriching gases. The liquid membranes involved in gas separation were provided by foam; an agglomeration of distorted gas bubbles in which the bubbles of gas are separated from each other by thin liquid films. Separation occurs due to differences in the solubilities and diffusivities of the various species of the gas mixture through the films. One of the ways by which separation is achieved is by generating a foam using the gas mixture and passing large bubbles of carrier gas through the foam. Different rates of diffusion of various species from the foam to the carrier bubble result in separation. This was the method used by Li[1] to demonstrate the use of foam for gas separation.

In order to predict the separation quantitatively, it is necessary to be able to predict the sizes of the bubbles generated when a carrier gas is injected from a nozzle into the moving foam. Up to this time, no such study has been reported in literature. The present study was therefore undertaken with a view to develop models for predicting the sizes of bubbles formed in foam which was moving parallel to the axis of the bubble forming nozzle. Theoretical estimates of bubble sizes given by these models are compared with the experimentally obtained values so as to arrive at that model which can describe bubble formation phenomenon in foam most appropriately.

2. Experimental

Though the basic mechanism of bubble formation in all liquids is the same, the size of the bubble at detachment depends strongly on the physical and rheological properties of the continuous phase. Hence, it is required to have an understanding of the rheological nature of foam in the present study. The structure of foam imparts to it properties that are different from its constituent components. Foam is a two-phase structure, made up of gas bubbles separated from each other by thin liquid films. The structure of foam can be idealised as an agglomeration of bubbles where each bubble is taken to be a pentagonal dodecahedron. This close-packed structure leads to restriction in the movement of individual bubbles. As a result, foam exhibits a yield stress, so that it behaves as a solid when stresses, less than the yield stress, act on it. Furthermore, foam also possesses a viscocity much higher than that of either of its constituent components. Both the yield stress and the viscocity of foam are functions of its hold-up for a fixed value of the average size of foam bubbles. The liquid hold-up is the volume fraction of liquid present in unit volume of foam. In the present study, it was therefore necessary to characterize the rheological properties with the liquid hold-up, as the foam bubble size was maintained constant. Experimental studies were performed to estimate these properties, namely, the yield stress and the effective viscosity as functions of the liquid hold-up of foam.

Experiments were also performed to measure the sizes of individual bubbles released in foam moving upwards. For this purpose, a column of dimensions 0·9m × 292 mm × 305 mm fabricated from perspex was employed. Arrangements were made to form foam within the column and to move the foam continuously at a given flow rate upwards through it. The foam was collected at the top of the column. It was broken there and the resulting liquid was re-fed into it at its base. In order to form foam, a 0·25 per cent solution of sodium lauryl sulphate was used, into which air was passed at the desired flow rate. Foam forming continuously at the surface of the surfactant solution thereby rose through the column at a steady rate. Variation of the flow rate of air enabled variation of the liquid hold-up of the foam generated. Bubbles of nitrogen were then introduced into the foam through a nozzle of diameter 2 mm.

3. Model development and verification

In general, experimental studies performed on bubble formation in liquids have been carried out under two conditions. These are the condition of constant gas flow rate (for which the pressure drop across the orifice is large enough so that the gas flow rate be independent of the size of the growing bubble), and the condition of constant chamber pressure (in which case the pressure upstream to the nozzle is maintained constant so that the flow rate of gas into the bubble varies as the bubble grows). In the present study, bubble formation was carried out under constant gas flow rate conditions.

Measurements of the bubble volumes were made as a function of: (i) liquid hold-up of foam, and (ii) rate of bubble-forming gas.

There are two main approaches of study regarding bubble formation in liquids. These are the approach of Davidson and Schuler[2] and the approach of Ramakrishnan *et al*[3] and Kumar[4] which have been proposed for both the conditions of constant gas flow rate and constant chamber pressure. These approaches were separately applied to the present study in order to develop a model describing bubble formation in moving foams, under conditions of constant gas flow rate. Three models were proposed. Model I is based on the approach of Davidson and Schuler, while Models II and III follow the approach of Kumar. In arriving at these models, it has been assumed that the rheology of foam conforms to that of a simple Bingham plastic for the conditions employed in the present study.

Model I which is based on the assumptions of Davidson and Schuler for bubble formation under conditions of constant gas flow rate considers the bubble to form from a point source with its centre initially present at the nozzle. Thus, according to this approach, the source is enveloped by the bubble during the process of growth. Detachment is assumed to occur when the bubble base covers a distance equal to its radius. In applying this model to the present case, there are two different situations. Since foam possesses a yield stress, the bubble will either be detached into foam and will move with a velocity different from foam if it has overcome the yield stress of foam or it will move at the velocity of foam if released when it has not overcome the yield stress. The latter case prevails when the bubble is detached before it attains enough buoyancy to counter the yield stress of foam. It was possible to estimate the volume the bubble should attain to just overcome the yield stress of foam (of a particular liquid hold-up). It was found that in the present case, the bubble size (for the conditions employed in this study) was always less than the volume required to counter the yield stress of the surrounding foam. Thus the bubble moved with the velocity of the foam throughout its formation time. It detached into the foam when the condition of detachment (mentioned above) was satisfied. Estimations of the bubble size according to this model gave much higher bubble volumes as compared to those obtained from experimental studies.

Models II and III are based on the approach of Ramakrishnan *et al*[3] and Kumar[4]. Model II is based on the two-stage concept of bubble formation of the above-mentioned authors. These authors considered bubble formation to take place in two stages, *viz.*, the expansion stage and the detachment stage. During the former stage, the bubble expands while its base remains fixed at the orifice. The end of the first stage is brought about when the net upward force acting on the bubble is equal to the net downward force on it. Thereafter, the bubble base lifts off the orifice. During the second stage, therefore, the bubble centre moves with a net velocity equal to the sum of the velocity of the base and the velocity of expansion since, during this time, the bubble is also expanding due to incoming gas. The bubble sizes estimated using Model II are found to be much higher than those obtained experimentally. Model III is arrived at by considering a modification of the two-stage process and corresponds to the first stage of the unified model of Kumar[4]. The predictions of this model are found to be in reasonable agreement with experimental results.

References

1. Li, N N	*Liquid membrane foam diffusion*, US patent, 3, 650, 091, 1972.
2. Davidson, J. F and Schuler, B O. G	Bubble formation at an orifice in an inviscid fluid, *Trans. Instn Chem Engr* 1960, **38**, 335–342.
3 Ramakrishnan, S., Kumar, R and Kuloor, N R	Studies in bubble formation–I Bubble formation under constant flow conditions, *Chem Engng Sci.*, 1969, **24**, 731–747
4. Kumar, R.	A unified approach to bubble and drop formation, *Chem. Engng Sci.*, 1971, **26**, 177–184

Thesis Abstract (M.Sc. (Engng))

Analysis of transients in a canal network by Rajeev Misra.
Research supervisors: K. Sridharan and M. S. Mohan Kumar.
Department: Civil Engineering.

1. Introduction

Generally, canals are designed based on uniform flow (steady flow) criterion coupled with regime concepts. But the uniform flow at all locations in the network is not feasible. The gradually varied steady-flow analysis is not simple due to unknown discharge distribution. Transients are introduced in the network due to operation of controls, used to regulate/distribute water. Opening of a gate may cause over topping, though for short durations, at several locations in the network leading to embankment erosion. Rapid drawdown in water levels resulting from gate closure may lead to embankment failure by sliding. Unlike river systems the effects of wave reflection from controls and branches may be of interest. So far no attention has been paid to the transient effects of control structure operations, such as time taken by the first water to reach a particular location and for it to stabilize the supplies. This kind of information may be useful, for instance, in minimizing wasteful drainage during night irrigation.

The present study is concerned with the analysis of transients in a canal network due to operation of control structures. The analysis is done through a numerical model based on Saint–Venant[1] equations of one-dimensional unsteady flows in open channels. The transient effects due to different types, locations and operation of control structures are studied. Results are obtained for a three level of canal system which may be looked upon as comprising main canal, branch canals and distributaries. The unsteady flow algorithm is also used to obtain non-uniform, steady-state variations of depth and discharge in the network, once the control structures are maintained at stationary positions.

2. Methodology

The problem of transients in channels is an initial boundary-value problem. The equations of one-dimensional unsteady flow are solved numerically along with initial and boundary conditions using the method of finite differences. For the analysis, explicit characteristic rectangular grid method using space-line interpolation scheme bounded by classical Courant stability criterion is used. The second stability criterion, 'Koren's stability'[2], is relaxed by taking the friction term and coefficients semi-implicitly.

The boundaries (ends of each canal) have been classified depending upon their nature and/or governing equations into four subgroups. The internal boundary conditions in the network, applicable at canal junctions, have been grouped into three types taking into account different combinations of boundaries. The computational nodes have been identified as interior nodes, junction nodes and network boundary nodes. The mathematical formulation, set of governing equations and solution methodology at different nodes are presented. The initial condition is taken as steady state gradually varied flow in the network. An algorithm based on uniform and gradually varied flow principles is developed to calculate, approximately, steady-state flow in the channel network, which is used to provide initial conditions for some of the problems studied

3. Computational procedure

The unsteady flow simulation at the current time at each node requires the solution of a set of nonlinear algebraic equations. This is in view of the fact that the friction term and coefficients are taken semi-implicitly and the control structure equations which are nonlinear are written at the current time level. All the sets of nonlinear equations are solved by Newton iterative method.

4. Software development

A general-purpose software has been developed in Pascal using the concepts of top-down design, and structured programming, using pseudo-code as design and development tool. To give a clear insight to the formulation and solution techniques, high-level pseudo code listings of the input data structure, main program and principal procedures are presented.

5. Application

The results of the analysis made for 12 different problems on a three-level canal network are presented in the form of depth and discharge hydrographs and water surface profiles. The network has five canals of trapezoidal shapes with different lengths (ranging from 4000 to 700 m), bed widths (10 to 2 m) side slopes (2:1 to 1·5:1), bed slopes ($1{\cdot}33^* \, 10^{-4}$ to $1^* \, 10^{-3}$) and Mannings n (0·015 to 0·03). It has two canal junctions of three canals each and four external network boundaries. The problems involve the study of transient effects due to opening and closing of gates at (a) the headworks, (b) second-level canal, (c) third-level canal, and (d) tail end, with different tail-end and junction boundary conditions. The transient effects due to a linearly rising wave at canal headworks are also studied.

6. Results and discussion

It is shown that the present unsteady flow algorithm can be used to obtain steady-state flow in a network for fixed position of control structures. Computations show that a significantly large time is required for the dissipation of transient effects due to gate operations. For gate operations of 900 s or lower considered in the study problems, it is found that steady flow is not reached, even after 20000 s in some cases. In general, it is observed that the final steady state is reached faster in case of gate opening or start up of the canal system than gate closure or shut-down of the system.

The transient effects due to gate operations at different locations in the network are discussed, with reference to relative variations in depth and discharge in various parts of the network. It was found that the depth hydrograph for a negative wave in any canal is flatter than the depth hydrograph for a positive wave, similar to the recession limb of a flood hydrograph. This feature is not so prominent in the case of discharge hydrographs. The wavefronts for positive waves created by gate opening are steeper than the wavefronts for negative waves created by gate closure. It was also observed that the waves moving downstream move faster in main canal than in smaller secondary canals.

It is demonstrated that the present model can handle complex situations that may arise from multiple gate operations. A problem is studied wherein three gates at different locations are operated with small time lags involving transient changes in boundary condition from gate discharge equation to junction energy equation and back, leading to large and rapid fluctuations in depth and discharge.

References

1 Chow, V. T.	*Open channel hydraulics*, 1959, McGraw-Hill
2 Huang, J and Song, C C S	Stability of dynamic flood routing schemes, *Proc J Hydraulics Div., ASCE*, 1985, **111**, 1497–1505

Thesis Abstract (M.Sc. (Engng))

A study on bandpassed speech from the point of intelligibility by C. N. S. Ganesh Murthy.
Research supervisors: M. Satyam and K. Ramkumar.
Department: Electrical Communication Engineering.

1. Introduction

Speech has been the subject of interest for a very long time. Even with so much advancement in processing techniques and in the understanding of the source of speech, it is, even today, rather difficult to generate speech in the laboratory in all its aspects. A simple aspect like how the speech can retain its intelligibility even if it is distorted or bandpassed is not really understood. This work deals with one small feature of speech, *viz.*, the intelligibility of speech is retained even when it is bandpassed with a minimum bandwidth of around 1 KHz located anywhere on the speech spectrum of 0–4 KHz.

Several experiments have been conducted by earlier workers by passing speech through various distortors like differentiators, integrators and infinite peak clippers and it is found that the intelligibility is retained to a very large extent in the distorted speech[1-5]. The integrator and the differentiator remove essentially a certain portion of the spectrum. Therefore, it is thought that the intelligibility of the speech is spread over the entire speech spectrum and that the intelligibility of speech may not be impaired even when it is bandpassed with a minimum bandwidth and the band may be located anywhere in the speech spectrum. To test this idea and establish this feature, if it exists, preliminary experiments have been conducted by passing the speech through different filters and it is found that the conjecture seems to be on the right line.

2. Experimental set-up

To carry out systematic experiments on this, an experimental set-up has been designed and fabricated which consists of a microprocessor-controlled speech recording, storing and speech playback system. Also, a personal computer is coupled to the microprocessor system to enable the storage and processing of the data. Thirty persons drawn from different walks of life like teachers, mechanics and students have been involved in collecting the samples and for recognition of the information of the processed speech. Even though sentences like 'This is Devices Lab' are used to ascertain the effect of bandwidth on intelligibility, for the purpose of analysis, vowels are used as speech samples.

3. Experiments

The experiments essentially consist of recording words and sentences spoken by the 30 participants and these recorded speech samples are passed through different filters with different bandwidths and central frequencies. The filtered output is played back to various listeners and observations regarding the intelligibility of the speech are noted. The listeners do not have any prior information about the content of the speech. It has been found that in almost all (95 per cent) cases, the messages or words are intelligible for most of the listeners when the bandwidth of the filter is about 1 KHz and this is independent of the location of the passband in the spectrum of 0–4 KHz.

4. Analysis

To understand how this feature of speech arises, spectra of vowels spoken by 30 people have been calculated using FFT algorithms on the digitized samples of the speech. It is felt that there is a cyclic behavior

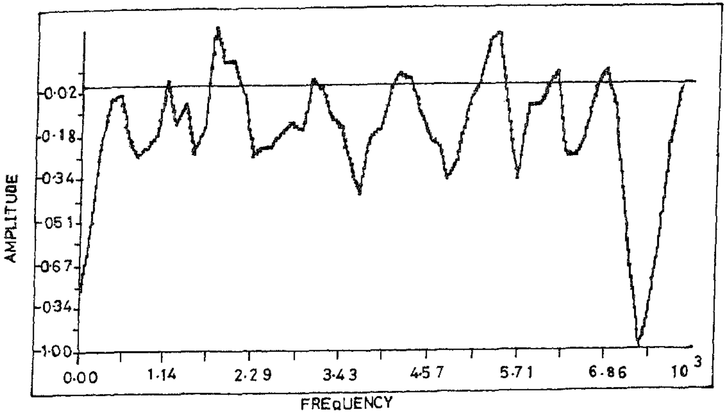

FIG. 1. Smoothened real part of the spectrum of vowel E, sample 2.

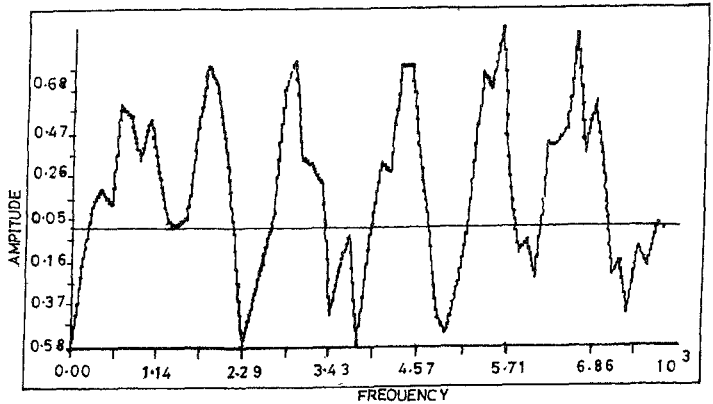

FIG. 2. Smoothened real part of the spectrum of vowel u, sample 1.

of the spectrum in all the samples. To make sure that the periodicity is present and also to arrive at the periodicity, a moving average procedure is employed to smoothen the spectrum. The smoothened spectra of all the vowels indeed show a periodicity of about 1 KHz. Figures 1 and 2 give typical smoothened

Table I

Mean periodicities of each of the vowels for each person

No	*A*	*E*	*I*	*O*	*U*
1	1·014	1·129	0·955	0·951	0·806
2	1·124	1·038	1·101	1·161	1·124
3	1·193	0·985	1·069	1·083	1·187
4	1·046	0·972	0·935	1·087	0·942
5	1·161	0·995	1·075	1·166	0·860
6	1·104	0·915	0·991	0·974	1·062
7	0·959	1·296	1·010	1·070	1·027
8	1·236	1·078	1·048	1·277	1·037
9	0·929	1·242	1·032	1·172	1·107
10	1·263	0·943	0·996	1·064	1·083
11	1·000	1·045	1·032	1·069	0·862
12	0·919	1·102	0·862	0·951	0·854
13	0·991	0·864	0·958	1·071	0·903
14	0·963	1·138	1·002	1·027	0·774
15	1·037	0·940	1·028	0·976	0·860
16	1·139	1·226	1·107	0·967	1·169
17	0·991	1·060	1·215	1·247	0·915
18	1·087	1·000	0·987	0·935	0·922
19	0·935	1·088	1·073	1·037	0·888
20	1·053	1·123	1·215	1·080	1·258
21	1·017	1·037	1·012	1·023	0·887
22	1·037	0·963	1·069	0·967	1·027
23	0·986	1·226	1·037	0·967	0·992
24	1·027	0·801	0·931	1·000	1·161
25	0·967	1·091	1·091	1·102	1·121
26	0·954	0·987	0·884	1·139	0·967
27	1·204	1·177	1·092	1·139	0·846
28	0·862	0·838	1·188	1·084	1·226
29	0·903	0·756	0·967	0·972	1·199
30	1·007	1·032	1·059	1·232	1·032

Table II

Mean of the periodicities

Vowel	*Mean (Hz)*
A	1040
E	1036
I	1037
O	1070
U	1009

spectra. Smoothing is performed using a windowsize of 200 samples and the smoothened samples are calculated at an interval of 50 samples. Table I gives the mean of each of the vowels for 30 persons. Table II gives the mean of the values of Table I. When the periodicities are analysed the average value of the periodicities has been found to be 1038 Hz with a standard deviation of 19 Hz (with respect to Table II). In view of this it is thought that the acoustic source responsible for speech must have generated this periodic spectrum, which might have been modified periodically to imprint the intelligibility. If this is true, one can perhaps easily understand this feature of the speech, *viz.*, the intelligibility is retained in a bandpassed speech of bandwidth 1 KHz, the passband located anywhere in the speech spectrum of 0–4 KHz.

5. Conclusion

Even though the analysis of the speech spectrum indicates a cyclicity, thus hinting that a cyclic frequency spectrum is perhaps responsible for the above observation, it is interesting to investigate as to how the basic spectrum arises from the mechanism of speech production and to show that the intelligibility modulation of the spectrum is also repeated in a cyclic way so that any portion of the spectrum in a bandwidth of 1 KHz can retain good intelligibility

References

1. Pollack, I. — Effects of high pass and low pass filtering on the intelligibility of speech in noise, *J Acoust. Soc. Am.*, 1948, **20**, 259–266.
2. Licklider, J. C. R. and Pollack, I. — Effects of differentiation, integration, and infinite peak clipping upon the intelligibility of speech, *J. Acoust. Soc Am.*, 1948, **20**, 42–51.
3. Egan, J. P and Wiener, F. M — On the intelligibility of bands of speech in noise, *J Acoust. Soc Am.*, 1946, **18**, 435–441.
4. Rabiner, L R and Schafer, R W. — *Digital processing of speech signals*, 1979, Prentice-Hall.
5. French, N. R and Steinberg, J C. — Factors governing the intelligibility of speech sounds, *J. Acoust. Soc Am*, 1947, 19, 90–119.

Thesis Abstract (M.Sc. (Engng))

A PC-8086-based scheme for automation of a mass spectrometer by P. V. Ramakrishnan.
Research supervisor: A. G. Menon.
Department: Instrumentation and Services Unit.

1. Introduction

Computers were first attached to mass spectrometers for data acquisition, reduction and presentation and to improve the efficiency of calculations. Later, mass spectrometers were controlled by making use of the capability of the computer to provide analog and digital signals. Scanning of the magnetic and electric field for focusing the mass-separated ions[1], switching of magnetic and electric fields for linked scans[2], for controlling the ion current and electron multiplier voltage[3] are some of the applications where computer control has been used. The schemes and hardware used in all these cases varied and were dependent upon specific applications. Although several computer-controlled mass spectrometers of foreign make are marketed, independent control and data-acquisition systems for existing and older mass spectrometers are not as easily found. Moreover, the interface cards on personal computers, which may be configured for specific control applications, put serious demands on the requirement of compatible interfaces on power supplies of older instruments for executing control. This work, consequently, aims at the development of the hardware and software schemes which may be easily adopted for automation of such instruments.

2. The control strategy

To evolve a generalized strategy for automation of mass spectrometers, a home-made thermal ion source mass spectrometer available in the laboratory was chosen. The home-made mass spectrometer consists of a triple-filament thermal ion source, a 90° magnetic sector analyser and an electron multiplier detector. Being a home-made instrument, the power supplies have been procured from various sources and they lack the conventional computer-compatible inputs which impede direct coupling either to a microprocessor or to a personal computer. Of the five power supplies that require control, only two filament power supplies (which float at the high acceleration voltage) and magnet power supply (which is scanned for obtaining the mass spectrum) are controlled since the high voltage and electron multiplier voltage power supplies are held constant.

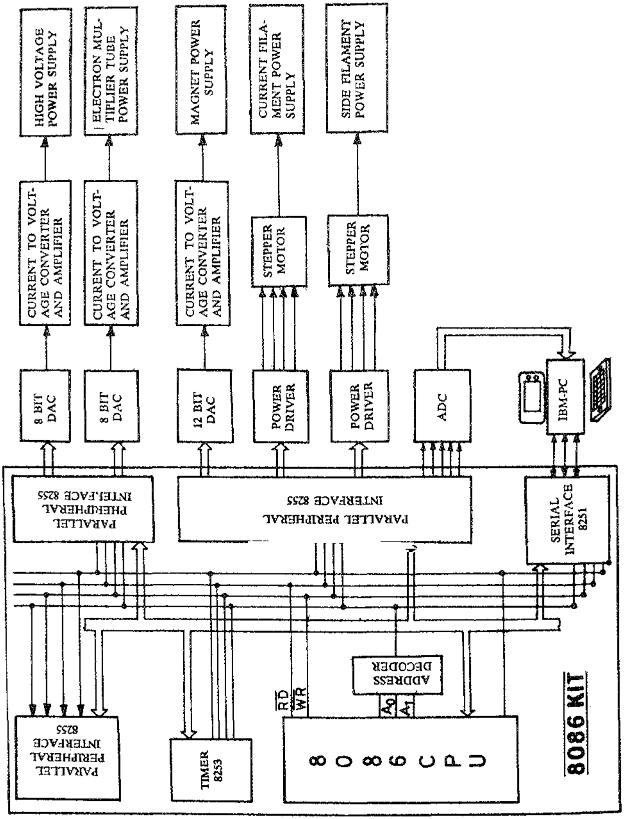

FIG. 1. Block diagram of hardware.

2.1. *Hardware*

The hardware configuration for the control of the two-filament power supplies and the magnet power supply and for data acquisition involves the use of an IBM PC-compatible personal computer and a standard inexpensive 8086 trainer kit linked together (serially) in a master–slave mode (Fig. 1).

The PC, which constitutes the front end, has been used principally to obtain information from the operator on the nature of control of the power supplies and to download this information on to the 8086 kit which executes the routine control operations. At the end of the control operation, the user is informed, through the monitor of the PC, that the data can be acquired. The advantage with the present scheme is that the PC is relieved of all routine control actions after the download operation and is used next only when data has to be acquired and processed.

The filament power supplies, which float at the high acceleration voltage, are controlled by stepper motors with their shafts isolated while the magnet power supply is controlled with 12-bit digital-to-analog converter. Data acquisition is done by the PC using an 8-bit analog-to-digital converter. The timer, 8253, available on the 8086 microprocessor kit generates the timings so that controls of the various power supplies can be performed at appropriate times.

2.2. *Software*

The software that has been developed for the purpose of control and data acquisition consists of: i) SPEC: a program in Pascal (run on the PC) which interacts with the user of the mass spectrometer to ascertain from him the various voltages, currents and magnetic fields that have to be output, the times at which the operation has to be performed and the nature of control, ii) CONTROL: a program in assembly language that operates (from the kit) on the data provided by the user through SPEC program and outputs the various parameters at appropriate times ensuring that no clash of timings (that may lead to the collapse of the entire control action) occurs, iii) DATACQ: a program in assembly language to acquire the data generated and store it in the memory area of PC, and iv) DNLOAD: the download program[4], in assembly language, has been modified for purposes of communication between the kit and PC before and after the control action.

The viability of the scheme to give day-to-day and single-run reproducibilities has been tested by measurement of isotopic ratios of ^{85}Rb/^{87}Rb in a sample of rubidium chloride.

References

1. Green, L. W., Barsczewski, J. S and Elliot, N. L — A versatile low-cost automation system for thermal ionization mass spectrometers, *Int J. Mass Spectrometry Ion Processes*, 1985, **67**, 253–265.

2. Borphy, J. J., Kingston, E. E., Morgan, J. T. and Nelson, D. — Microprocessor controller for linked scans of electric sector voltage and magnetic field in a magnetic double focusing mass spectrometer, *Int J. Mass Spectrometry Ion Processes*, 1980, **35**, 319–334.

3. Servais, Ch , Locht, R. and Momigny, J — Versatile low-cost automation system for an electro-ionization source, *Int J Mass Spectrometry Ion Processes*, 1986, **74**, 179–196

4. Hall, D. V. — *Microprocessors and interfacing. Programming and hardware*, 1987, McGraw-Hill.

Thesis Abstract (M.Sc. (Engng))

Studies on fatigue, corrosion and corrosion-fatigue of ductile irons by S. Muthukumaraswamy.

Research supervisor: S. Seshan.
Department: Mechanical Engineering.

1. Introduction

Within a span of four decades from its introduction, ductile iron has become one of the most widely used engineering materials. Even though ductile iron has the same composition as grey iron so far as the starting material is concerned, there is appreciable variation in processing. Consequently, graphite in ductile iron is present as well-formed nodules which result in enhanced mechanical properties. The properties of ductile iron can vary over a wide spectrum depending upon the matrix structure. Either by judicious alloying or by selective heat treatment, different matrix structures can be obtained in ductile irons. The mechanical properties of ductile iron are controlled by steel-like matrix rather than graphite.

Fatigue is the phenomenon which causes failure when a component is subjected to repeated loading at stress levels lower than the ultimate strength of the material. The deterioration of a material due to its interaction with the environment (either chemically or electrochemically) is known as corrosion. When a component is subjected to fatigue loading in a corrosive atmosphere, the combined action of corrosion and fatigue is much more detrimental than when they are acting individually. The cumulative action of the corrosion and fatigue on the material is generally termed as corrosion-fatigue.

There has been an increasing trend towards the use of ductile iron castings in applications involving fatigue loads, many of them involving corrosive environment. It is seen that the available data on the fatigue properties of ductile irons is rather limited. In particular, the effect of corrosion on the fatigue behaviour of ductile irons has not been considered in any depth. Therefore, a systematic study was undertaken to evaluate the effect of matrix structure and corrosion on the fatigue properties of ductile irons.

2. Experimental details

Desulphurised pig iron was used as the base material in this investigation for the production of ductile iron melts. The Y-block test casting selected was based on ASTM standard A536-72 specified for ductile iron. Melting was accomplished in a Birlec-make, direct act furnace. The nodularizing treatment for obtaining spheroidal form of graphite was carried out using sandwich technique employing Ni–Mg master alloy. The melts were subjected to post-inoculation subsequent to the nodularizing treatment.

Test blanks cut from solidified castings were then subjected to various heat treatments following different cycles to obtain the desired matrix structure, *viz.*, ferrite, pearlite, martensite and bainite. From the test castings subjected to various heat treatments, specimens were machined out and subjected to microstructural studies, assessment of tensile and fatigue properties, corrosion studies and corrosion fatigue studies.

3. Results and discussion

The investigation carried out to characterize ductile irons with different matrices for fatigue, corrosion and corrosion fatigue have led to the following inferences.

3.1. *Fatigue*

It has been observed that in ductile irons fatigue strength is mostly dependent on hardness. In addition, any increase in tensile strength normally leads to an increase in fatigue strength. On the other hand, endurance ratio follows the trend of variation of ductility. The fatigue strength of ductile irons with different matrix structures varies from a low value of 240 MPa to a high value of 510 MPa.

3.2. *Corrosion*

Corrosion behaviour of ductile irons does not seem to be dependent on the matrix structure. Corrosion rates assessed using salt spray chamber have been found to be more or less the same for ductile irons with all the different matrices in both the environments tested (*viz.*, 3% NaCl and 5% HCl). However, acid medium is much more corrosive than salt medium.

The electrochemical potential of ductile irons with different matrices differs considerably from each other, indicating that a different mechanism is involved in the corrosion process. Based on the electrochemical potential of the matrix, structure, ductile irons can be rated as follows:

Martensitic	Noble
Ferritic	Less noble
Bainitic	Active
Pearlitic	Most active

Such a variation is attributed to the presence of more than one phase.

3.3. *Corrosion-fatigue*

Fatigue properties, namely, fatigue strength and endurance ratio, of ductile irons get drastically reduced in the presence of a corrosive environment. Such an effect is much more severe in acidic medium compared to salt water environment. It appears that the corrosion fatigue strength of ductile irons cannot be increased appreciably by changing the matrix alone or by increasing the tensile strength. Probably, the effective method would be to resort to alloying.

The fatigue behaviour of ductile irons in corrosive environment (in particular 3% NaCl medium) is akin to that of non-ferrous metals in air wherein the fatigue life registers an increase with decrease in applied stress level.

This investigation reveals that fatigue properties of ductile irons are drastically reduced in corrosive environments. In view of the above, due consideration should be given to the corrosion fatigue strength while designing ductile iron components which are likely to be exposed simultaneously to fatigue and corrosion in service.

References

1. Ikawa, K. and Ohira, G.	Fatigue properties of cast irons in relation with graphite structure, *Cast Metals Res. J.*, 1967, **3**, 11–21.
2. Eagan, T E.	Fatigue strength of nodular iron tested, *Iron Age*, 1951, **168** **(24)**, 136–139.
3. Skold, R V. and Larson, T. E.	Measurement of instantaneous corrosion rate by means of polarization data, *Corrosion*, 1957, **13**, 139t–142t.
4. Collins, H. H.	Corrosion resistance of cast irons, *BCIRA J.*, 1963, **2**, 589–595
5. Hoeppner, D. W.	*Corrosion-fatigue consideration of material selection and engineering design*, NACE Publication No. 2, Paper No. 1, 1972.
6. Jaske, C. F.	*Corrosion fatigue of materials in marine environments*, 1976, Battelle Press, Geneva.